

Interpreting the cosmic far-infrared background anisotropies using a gas regulator model

Hao-Yi Wu,^{1,2★} Olivier Doré,^{1,2} and Romain Teyssier³

¹California Institute of Technology, MC 367-17, Pasadena, CA 91125, USA

²Jet Propulsion Laboratory, 4800 Oak Grove Drive, Pasadena, CA 91109, USA

³Institute for Computational Science, University of Zurich, CH-8057 Zürich, Switzerland

6 June 2022

ABSTRACT

Cosmic far-infrared background (CFIRB) is a powerful probe of the history of star formation rate and the connection between baryons and dark matter. In this work, we explore to which extent the CFIRB anisotropies can be reproduced by a simple physical framework for galaxy evolution, the gas regulator (bathtub) model. The model is based on continuity equations for gas, stars, and metals, taking into account cosmic gas accretion, star formation, and gas ejection. Our model not only provides a good fit to the CFIRB power spectra measured by *Planck*, but also agrees well with the correlation between CFIRB and gravitational lensing, far-infrared galaxy number counts, and bolometric infrared luminosity functions. The strong clustering of CFIRB indicates a large galaxy bias, which corresponds to haloes of mass $10^{12.5}M_{\odot}$ at $z = 2$; thus, CFIRB favors strong infrared emission in massive haloes, which is higher than the expectation from the star formation rate. We provide constraints and fitting functions for the cosmic star formation history and the infrared luminosity–halo mass relation.

Key words: galaxies: haloes — galaxies: star formation — submillimetre: diffuse background — submillimetre: galaxies

1 INTRODUCTION

Cosmic far-infrared background (CFIRB) originates from unresolved dusty star-forming galaxies across cosmic time. In these galaxies, the ultraviolet (UV) photons associated with newly formed, massive stars are absorbed by dust and re-emitted in far-infrared (FIR), and the FIR emissions serve as an indicator of the star formation rate (SFR). At the FIR wavelengths ($\sim 100\ \mu\text{m}$ to 1 mm, also known as submillimetre), most galaxies are unresolved and can only be observed as background intensity fluctuations. These fluctuations contain information about the cosmic star formation history, as well as the dark matter haloes in which the dusty star-forming galaxies are located. Compared with UV, the star formation history from FIR is much less explored because of the low resolution; thus, CFIRB provides an important piece of the puzzle of the cosmic star formation history.

Predicted almost half a century ago (Partridge & Peebles 1967; Bond et al. 1986), the CFIRB was first discovered by *COBE*-FIRAS (Puget et al. 1996; Fixsen et al. 1998; Hauser et al. 1998; Gispert et al. 2000; Hauser & Dwek 2001) and subsequently observed by ISO (Matsuhara et al. 2000; Lagache & Puget 2000; Elbaz et al. 2002), *Spitzer* (Dole

et al. 2006; Grossan & Smoot 2007; Lagache et al. 2007), BLAST (Viero et al. 2009), SPT (Hall et al. 2010), ACT (Hajian et al. 2012), *Herschel* (Amblard et al. 2011; Berta et al. 2011; Viero et al. 2013a), and *Planck* (Planck Collaboration XVIII 2011; Planck Collaboration XXX 2014). In particular, the angular power spectra of CFIRB provide the luminosity-weighted galaxy bias and thus the information about the mass of the underlying dark matter haloes (e.g., Viero et al. 2013a; Thacker et al. 2013; Planck Collaboration XXX 2014).

To date, most of the interpretations of the CFIRB anisotropies have been based on phenomenological models with limited physical interpretation. For example, Addison et al. (2013) modeled the CFIRB and number counts using general parameterizations for the luminosity function, the spectral energy distribution (SED), and the scale-dependent galaxy bias. On the other hand, Shang et al. (2012) implemented a luminosity–mass relation in the halo model to improve the modeling at small scales (also see, e.g., Viero et al. 2009; Amblard et al. 2011; Planck Collaboration XVIII 2011; De Bernardis & Cooray 2012; Xia et al. 2012; Viero et al. 2013a). In addition, Planck Collaboration XXX (2014) provided updated measurements of the CFIRB power spectra as well as new constraints on linear and halo models; however, the star formation rate density inferred from their

★ Email: hywu@caltech.edu

halo model appears too high at high redshift when compared with UV observations.

In this work, we develop a physical model for the connection between dark matter haloes and dusty star-forming galaxies. We constrain this model using CFIRB measured by *Planck*. We then validate our model with a comprehensive comparison to FIR/submm galaxy observations. Our model provides a simple, physically-motivated framework to compare and interpret various FIR observations.

We apply the gas regulator model, which is based on the continuity equations of gas, stars, and metal (also known as the bathtub or reservoir model, see, e.g., Bouché et al. 2010; Lilly et al. 2013; Dekel et al. 2013; Dekel & Mandelker 2014). We then apply the halo model for calculating the power spectra of CFIRB (Scherrer & Bertschinger 1991; Seljak 2000; Cooray & Sheth 2002). We fit the model to the CFIRB anisotropies measured by *Planck* (Planck Collaboration XXX 2014) and the total intensity measured by COBE-FIRAS (Fixsen et al. 1998). Our model agrees well with various IR observations, as well as the cosmic star formation rate density and cosmic dust mass density constrained by other observations. We find that CFIRB requires high IR luminosity for massive haloes ($L_{\text{IR}} \sim 10^{12} L_{\odot}$ for haloes of mass above $10^{13} M_{\odot}$); this result is consistent with earlier findings (e.g., Shang et al. 2012; Addison et al. 2013; Béthermin et al. 2013) but is in excess compared with the SFR constrained by UV, optical, and near-infrared (NIR). This excess of IR luminosity can be related to heating by old stars or dust-obscured active galactic nuclei.

This paper is organized as follows. Section 2 describes the gas regulator model and provides a quasi steady-state solution relevant for SFR and dust property. In Section 3, we incorporate the gas regulator model into the halo model to calculate observed quantities. In Section 4, we fit our model to the CFIRB angular power spectra and intensity. Section 5 shows comparisons between our model and other infrared observations. In Section 6, we discuss the implications of our model, including the galaxy–halo connection and the cosmic star formation history. We summarize in Section 7.

Throughout this paper, we use a flat Λ CDM cosmology based on the *Planck* 2013 results (Planck Collaboration XVI 2014); $\Omega_M = 0.31$; $\Omega_{\Lambda} = 0.69$; $h = 0.67$. We use the linear matter power spectrum at $z = 0$ calculated by CAMB (Lewis et al. 2000) with $\Omega_b h^2 = 0.022$; $\Omega_c h^2 = 0.12$; $n_s = 0.96$; $A_s = 2.215 \times 10^{-9}$. When converting SFR to IR luminosity, we use $L_{\text{IR}} = \text{SFR}/K$, where $K = 1.7 \times 10^{-10} M_{\odot} \text{yr}^{-1} L_{\odot}^{-1}$ based on the Salpeter initial mass function (Kennicutt 1998).

2 GAS REGULATOR MODEL FOR GALAXY EVOLUTION

In the gas regulator model, a galaxy is assumed be a reservoir of gas, stars, and metal; the mass of each component is determined by a continuity equation with sources (cosmic accretion), sinks (star formation), and outflow. This model assumes that both the star formation rate and the gas outflow rate are proportional to the gas mass; therefore, the system is self-regulated and will eventually reach a steady state (e.g., Bouché et al. 2010; Lilly et al. 2013; Dekel et al. 2013). Our model is based on the minimal implementation in Dekel & Mandelker (2014, DM14 thereafter) with various

modifications. Table 1 summarizes the physical processes in this model, and Table A1 lists the parameters in this model.

2.1 Basic model and quasi steady-state solution

To describe the source terms, let us denote the cosmic accretion rate of *all* baryon mass as \dot{M}_a . In this accreted baryon mass, we assume that the gas mass fraction is f_{ga} , and the stellar mass fraction is $(1 - f_{\text{ga}})$. Star formation converts gas mass to stellar mass. We denote the SFR of the galaxy as \dot{M}_{sf} ; since stars return a fraction (denoted as R) of the gas to the reservoir, the gas consumption rate is given by $(1 - R)\dot{M}_{\text{sf}}$. In addition, the gas mass can be ejected from the galaxy due to feedback processes, and we assume that the mass loss rate is proportional to the SFR, $\eta\dot{M}_{\text{sf}}$. Here η is the mass loading factor and will be discussed in detail in Section 2.3. We assume that the outflow of stellar mass is negligible.

The continuity equations of gas mass (M_g) and stellar mass (M_s) are given by

$$\dot{M}_g = f_{\text{ga}}\dot{M}_a - (1 - R + \eta)\dot{M}_{\text{sf}}, \quad (1)$$

and

$$\dot{M}_s = (1 - f_{\text{ga}})\dot{M}_a + (1 - R)\dot{M}_{\text{sf}}. \quad (2)$$

Since the stellar mass is not directly observable in FIR, we will not further discuss the stellar mass in this paper.

We assume that the cosmic accretion provides negligible metal mass. The metal production rate is given by $y(1 - R)\dot{M}_{\text{sf}}$, where y is the metal yield¹. The loss of metal is proportional to the loss of gas. The continuity equation of metal mass (M_m) is thus given by

$$\dot{M}_m = y(1 - R)\dot{M}_{\text{sf}} - (1 - R + \eta)\dot{M}_{\text{sf}} \frac{M_m}{M_g}. \quad (3)$$

For the quasi steady-state solution, we assume $\dot{M}_g = 0$ and $\dot{M}_m = 0$. Equations 1 and 3 become

$$\dot{M}_{\text{sf}} = \frac{f_{\text{ga}}\dot{M}_a}{1 - R + \eta} \quad (4)$$

and

$$M_m = M_g \frac{y(1 - R)}{1 - R + \eta}. \quad (5)$$

Under this assumption, the gas metallicity M_m/M_g is constant with time.

To calculate the gas mass, we assume that $\dot{M}_{\text{sf}} = M_g/t_{\text{sf}}$, where t_{sf} is the star formation time scale,

$$M_g = \frac{f_{\text{ga}}\dot{M}_a t_{\text{sf}}}{1 - R + \eta}. \quad (6)$$

2.2 Implementation

Equation 4 is our prediction for the star formation rate. We assume that the baryon mass accretion rate \dot{M}_a is proportional to the dark matter accretion rate

$$\dot{M}_a = f_b p \dot{M}_h, \quad (7)$$

¹ In this work, we define the metal yield y as the ratio between the metal mass returned to the gas and the stellar mass locked in stars (e.g., Schneider 2010).

Physical process	Gas	Star	Metal in gas
Cosmic accretion	$f_{\text{ga}}\dot{M}_{\text{a}}$	$(1 - f_{\text{ga}})\dot{M}_{\text{a}}$	(Negligible)
Star formation	$-(1 - R)\dot{M}_{\text{sf}}$	$(1 - R)\dot{M}_{\text{sf}}$	$y(1 - R)\dot{M}_{\text{sf}} - (1 - R)\dot{M}_{\text{sf}}M_{\text{m}}/M_{\text{g}}$
Outflow	$-\eta\dot{M}_{\text{sf}}$	(Negligible)	$-\eta\dot{M}_{\text{sf}}M_{\text{m}}/M_{\text{g}}$

Table 1. Summary of source, sink, and outflow terms in the gas regulator model.

where M_{h} is the mass of the dark matter halo; f_{b} is the cosmic baryon mass fraction $\Omega_{\text{b}}/\Omega_{\text{M}}$, which is assumed to be 0.18 (Planck Collaboration XVI 2014); p indicates the mass fraction of the gas that can penetrate the halo and reach the galaxy.

For the mass accretion rate of dark matter haloes, we use the fitting formula calibrated using the two Millennium simulations by Fakhouri et al. (2010)

$$\dot{M}_{\text{h}} = 46.1 \text{M}_{\odot} \text{yr}^{-1} \left(\frac{M}{10^{12} \text{M}_{\odot}} \right)^{1.1} \times (1 + 1.11z) \sqrt{\Omega_{\text{M}}(1+z)^3 + \Omega_{\Lambda}}. \quad (8)$$

To improve the flexibility to the model, we include an extra redshift dependence in \dot{M}_{a}

$$f(z) = \begin{cases} \left(\frac{1+z}{1+z_0} \right)^{\delta_1} & \text{if } z \leq z_0 \\ \left(\frac{1+z}{1+z_0} \right)^{\delta_2} & \text{if } z > z_0. \end{cases} \quad (9)$$

We assume that \dot{M}_{sf} is proportional to the IR luminosity,

$$L_{\text{IR}} = \frac{\dot{M}_{\text{sf}}}{K}, \quad (10)$$

where $K = 1.7 \times 10^{-10} \text{M}_{\odot} \text{yr}^{-1} \text{L}_{\odot}^{-1}$ (Kennicutt 1998, based on the Salpeter initial mass function).

To summarize, the L_{IR} –halo mass relation is given by

$$L_{\text{IR}} = \frac{f_{\text{ga}} f_{\text{b}} p}{K(1 - R + \eta)} \dot{M}_{\text{h}} f(z). \quad (11)$$

We assume that the dust mass is proportional to the metal mass with a constant dust-to-metal ratio, $r = M_{\text{d}}/M_{\text{m}}$, and is given by

$$M_{\text{d}} = \frac{ry(1 - R)}{1 - R + \eta} t_{\text{sf}} \dot{M}_{\text{sf}} = \frac{ry(1 - R)}{(1 - R + \eta)^2} f_{\text{ga}} f_{\text{b}} p \dot{M}_{\text{h}} f(z) t_{\text{sf}}. \quad (12)$$

Following DM14, we assume that the star formation time scale is proportional to the dynamical time, $t_{\text{sf}} = \epsilon^{-1} t_{\text{d}}$, and $\epsilon = 0.02$. The dynamical time is assumed to be proportional to the cosmic time, $t_{\text{d}} = \nu t$, and $\nu = 0.0071$.

We assume that the spectral luminosity is given by an optically-thin modified blackbody with a single dust temperature T_{d} (e.g., Hayward et al. 2011)

$$L_{\nu} = 4\pi\kappa_{\nu} M_{\text{d}} B_{\nu}(T_{\text{d}}), \quad (13)$$

and that the opacity in IR follows a power-law

$$\kappa_{\nu} = \kappa_0 \left(\frac{\nu}{\nu_0} \right)^{\beta}. \quad (14)$$

Integrating L_{ν} over ν , we obtain L_{IR} as a function of M_{d} and T_{d} . Solving for T_{d} , we obtain

$$T_{\text{d}} = \frac{h}{k} \left[\frac{L_{\text{IR}} c^2 \nu_0^{\beta}}{\Gamma(4 + \beta) \zeta(4 + \beta) 8\pi\kappa_0 h M_{\text{d}}} \right]^{1/(4 + \beta)}. \quad (15)$$

Following Hayward et al. (2011), we assume that $\kappa_0 = 0.07 \text{m}^2 \text{kg}^{-1}$ at $850 \mu\text{m}$ at observed frame, $\nu_0 = 353(1 + z)$ GHz. The spectral index β is a free parameter in our model. Since we only concerns the FIR wavelengths in the Rayleigh–Jeans tail, we expect that the single-temperature modified blackbody is a good description for our SED.

2.3 Modeling feedback via mass loading factor

Equation 4 indicates that the star formation rate is determined by the mass accretion rate; however, additional feedback processes can affect the star formation rate. For low-mass haloes, supernova feedback can eject gas efficiently and suppress the star formation rate (e.g., Benson et al. 2003; Dutton & van den Bosch 2009). To model this effect, we assume $\eta \propto M_{\text{h}}^{-\alpha_1}$ for $M_{\text{h}} < M_{\text{pk}}$, where M_{pk} is the halo mass associated with the peak of the star formation efficiency.

Different values of α_1 correspond to different physical models for supernova feedback. For example, for energy-driven winds, $\eta \propto V_{\text{vir}}^{-2} \propto M_{\text{vir}}^{-2/3}$ (e.g., Benson 2010); for momentum-driven winds, $\eta \propto V_{\text{vir}}^{-1} \propto M_{\text{vir}}^{-1/3}$ (e.g., Murray et al. 2005; Hopkins et al. 2012); for constant winds, $\eta = \text{constant}$ (e.g., Springel & Hernquist 2003). Steeper scaling relations have also been adopted by some semi-analytical models (e.g., Guo et al. 2011).

Observations have been used to estimate the velocities of gas outflow; however, constraining the mass dependence of the mass loading factor is still challenging (e.g., Weiner et al. 2009; Chen et al. 2010; Martin et al. 2012; Rubin et al. 2014, see Veilleux et al. 2005; Erb 2015 for reviews). On the other hand, Lu et al. (2015) have used the galaxy stellar mass–metallicity relations to constrain the mass loading factor. Muratov et al. (2015) have used the FIRE simulations to characterized the mass loading factor as a function of stellar mass and redshift, and Hayward & Hopkins (2015) have developed an analytical model to describe how the mass loading factor depends on circular velocity and gas fraction.

For massive haloes, the star formation rate is suppressed by feedback from active galactic nuclei (e.g., Croton et al. 2006) or quenched due to environment (e.g., Wetzel et al. 2012). Thus, for massive haloes ($M_{\text{h}} > M_{\text{pk}}$), we phenomenologically model the mass loading factor as $\eta \propto M^{\alpha_2}$; this parameterization effectively describes the reduced supply of cold gas. In addition, observations have hinted that star formation rate and the AGN luminosity is related to each other (Lutz et al. 2010), supporting the gas regulator model in the regime of AGN feedback.

To make the transition between high- and low-mass smooth, we adopt the function form (see, e.g., [Feldmann 2015](#))

$$\eta(M) = f(x, y) = \eta_0 \left(1 + x + y - (1 + x^{-1} + y^{-1})^{-1} \right), \quad (16)$$

where

$$x = \left(\frac{M_h}{M_{pk}} \right)^{-\alpha_1}, \quad y = \left(\frac{M_h}{M_{pk}} \right)^{\alpha_2}. \quad (17)$$

We use four free parameters to describe the mass loading factor: (η_0 , α_1 , α_2 , $\log_{10} M_{pk}$).

3 HALO MODEL FOR CLUSTERING

Given the $L_{IR}-M_h$ relation and the SED from the gas regulator model, we can apply the halo model to calculate the CFIRB power spectra and various FIR observables. We follow the implementation of satellite galaxies in [Shang et al. \(2012\)](#). In addition, we include the scatter between IR luminosity and halo mass².

3.1 CFIRB Intensity and power spectra

We denote ν as the frequency in the *observed* frame. For brevity, we denote L_{IR} as L and M_h as M below. The emission coefficient at ν at redshift z is given by integrating the spectral luminosity of all haloes, described by the halo mass function (dn/dM), at this redshift,

$$j_\nu(z) = \int dM \frac{dn}{dM} [f_\nu^{\text{cen}}(M, z) + f_\nu^{\text{sat}}(M, z)], \quad (18)$$

where f_ν^{cen} and f_ν^{sat} corresponds to the contribution from central and satellite galaxies in a halo of mass M ,

$$\begin{aligned} f_\nu^{\text{cen}}(M, z) &= \frac{1}{4\pi} N_{\text{cen}} L_{(1+z)\nu}(M, z), \\ f_\nu^{\text{sat}}(M, z) &= \frac{1}{4\pi} \int dM_s N_s(M_s, M) L_{(1+z)\nu}(M_s, z). \end{aligned} \quad (19)$$

Here M_s denotes the mass of subhaloes, and dN_s/dM_s denotes the subhalo mass function in a halo of mass M . We assume that the luminosity of satellite galaxies is lower than that of central galaxies by a factor of q ,

$$L_{(1+z)\nu}(M_s, z) = q L_{(1+z)\nu}(M, z), \quad 0 \leq q \leq 1. \quad (20)$$

For the halo mass function, we use the fitting formula in [Tinker et al. \(2008\)](#); for the subhalo mass function, we use the fitting formula in [Tinker & Wetzel \(2010\)](#).

The spectral intensity is given by integrating the emission coefficient over all redshifts,

$$I_\nu = \int dz \frac{d\chi}{dz} a j(z), \quad (21)$$

where $a = 1/(1+z)$ is the scale factor, and χ is the comoving distance.

The angular power spectra at large scale are determined

by galaxy pairs in two different haloes, i.e., the two halo term, which is given by

$$C_{\ell, \nu\nu'}^{2h} = \int \frac{dz}{\chi^2} \frac{d\chi}{dz} a^2 B_\nu(z) B_{\nu'}(z) P_{\text{lin}}(k, z), \quad (22)$$

where B_ν also includes the contributions from central and satellite galaxies,

$$B_\nu(z) = \int dM \frac{dn}{dM} b(M) [f_\nu^{\text{cen}} + f_\nu^{\text{sat}}], \quad (23)$$

where $b(M)$ is the halo bias; we use the fitting function in [Tinker et al. \(2010\)](#).

The contribution by galaxy pairs in the same halo, i.e., the 1-halo term, is given by

$$C_{\ell, \nu\nu'}^{1h} = \int \frac{dz}{\chi^2} \frac{d\chi}{dz} a^2 A_{\nu\nu'}(k, z), \quad (24)$$

where

$$A_{\nu\nu'}(k, z) = \int dM \frac{dn}{dM} [f_\nu^{\text{cen}} f_{\nu'}^{\text{sat}} u + f_{\nu'}^{\text{cen}} f_\nu^{\text{sat}} u + f_\nu^{\text{sat}} f_{\nu'}^{\text{sat}} u^2]. \quad (25)$$

Here $u = u(k, M, z)$ is the halo mass density profile in Fourier space; we adopt the NFW profile ([Navarro et al. 1997](#)).

3.2 Spectral flux density function and shot noise

The spectral flux density is related to the spectral luminosity via

$$S_\nu = \frac{L_{(1+z)\nu}}{4\pi\chi^2(1+z)}. \quad (26)$$

We assume that at a given halo mass M , S_ν has the following probability distribution function

$$P(\ln S_\nu | M) = \frac{1}{\sqrt{2\pi}\sigma} \exp \left[-\frac{(\ln S_\nu - \langle \ln S_\nu \rangle)^2}{2\sigma^2} \right]. \quad (27)$$

We note that under this assumption

$$\langle \ln S_\nu \rangle = \ln \langle S_\nu \rangle - \frac{\sigma^2}{2}. \quad (28)$$

As we will see later, since σ is not negligible, $\langle \ln S_\nu \rangle \neq \ln \langle S_\nu \rangle$.

The contribution of the satellite galaxies to the flux function is small negligible. The flux density function is given by integrating over the halo mass function

$$\frac{dn}{d\ln S_\nu}(z) = \int dM \frac{dn}{dM} P(\ln S_\nu | \ln M). \quad (29)$$

The shot noise of the power spectra is calculated by integrating the square of the flux density for all galaxies,

$$C_{\nu\nu'}^{\text{shot}} = \int dz \frac{d\chi}{dz} \chi^2 \int d\ln S_\nu \frac{dn}{d\ln S_\nu} S_\nu S_{\nu'}. \quad (30)$$

For the shot noise in cross power spectra ($\nu \neq \nu'$), we assume

$$C_{\nu\nu'}^{\text{shot}} = \left(C_{\nu\nu}^{\text{shot}} C_{\nu'\nu'}^{\text{shot}} \right)^{1/2}. \quad (31)$$

This assumption is consistent with the cross shot noise found in [Planck Collaboration XXX \(2014\)](#).

² We note that in the presence of a scatter, all equations in Section 3.1 involve $\int LP(\ln L|M)d\ln L = \langle L \rangle$; therefore, all the equations in this section look the same as if there is no scatter.

4 FITTING MODEL TO CFIRB

We present the data sets we use, our fitting procedure, and the constraints on model parameters.

4.1 Observed CFIRB power spectra and intensity

We use the angular power spectra published in [Planck Collaboration XXX \(2014\)](#), which are based on maps measured in 4 frequency bands by *Planck* HFI: 217, 353, 545, and 857 GHz (1382, 849, 550, and 350 μm), for a total area of 2240 deg^2 . In particular, we used the 10 auto- and cross- spectra presented in Table D.2 in [Planck Collaboration XXX \(2014\)](#), which exclude the primordial cosmic microwave background, Galactic dust, and the thermal Sunyaev–Zeldovich effect. We use the multipoles $187 \leq \ell \leq 2649$; this leads to 83 data points in total. We use the color-correction factors given in Section 5.3 of [Planck Collaboration XXX \(2014\)](#).

We use the CFIRB intensity I_ν measured by *COBE*-FIRAS from [Fixsen et al. \(1998\)](#); in particular, we use the values and error bars quoted in Table 5 in [Planck Collaboration XVIII \(2011\)](#).

4.2 Fitting procedure

Our likelihood function $P(\mathbf{D}|\theta)$ is given by

$$-\ln P(\mathbf{D}|\theta) = \sum \frac{(D_i - M_i(\theta))^2}{\sigma_i^2}, \quad (32)$$

where D_i is a data point, σ_i is its error bar, and M_i is the model prediction based on a set of parameters θ . For the CFIRB intensity, D_i is νI_ν and σ_i is $\sigma(\nu I_\nu)$ for four frequency bands: (217, 353, 545, 857) GHz. For the CFIRB angular power spectra, D_i is $C_\ell^{\nu\nu'}$ and σ_i is $\sigma(C_\ell^{\nu\nu'})$ for 4 auto- and 6 cross- spectra, for ℓ between 187 and 2649.

We use the publicly available Markov chain Monte Carlo (MCMC) code *emcee* ([Foreman-Mackey et al. 2013](#)) Version 2.0.0 to explore the parameter space. In particular, *emcee* uses an ensemble of N walkers to update each other. Briefly, for a given walker at position X_k , the algorithm uses another walker $X_{j \neq k}$ to propose a new position $Y = X_j + Z[X_k - X_j]$, where Z is a random variable drawn from a distribution function that makes the proposal symmetric. The new position is accepted with a probability of $\min(1, Z^{N-1}p(Y)/p(X_k))$, where $p(x)$ is the posterior probability. We refer the readers to [Foreman-Mackey et al. \(2013\)](#) for the complete description of the algorithm.

We have 14 free parameters in the gas regulator model (see Table A2), 87 data points, and the χ^2 is 240 for 73 degrees of freedom. We use top-hat priors with generous ranges for all parameters. We have run 10 MCMC chains, each of which includes approximately 200,000 samples. We discard the first half of the chains as burn-in. We then apply the Gelman–Rubin diagnostic ([Gelman & Rubin 1992](#)), which compares the “within-chain variance” and the “between-chain variance” for multiple chains. We have ensured that the scale reduction factor $\sqrt{\hat{R}}$ is much less than 1.1. Figure A1 shows the posterior distributions from the MCMC chains. Table A2 shows the constraints on the model parameters, and Table A3 shows the correlation matrix for these parameters.

4.3 Best-fit model

Figure 1 shows the data and the best-fit model (with the maximum likelihood) for the CFIRB intensity (left panel) and the angular power spectrum at 545 GHz (550 μm , right panel). Figure B1 shows the full 10 auto- and cross-spectra from the 4 bands of *Planck*. For the CFIRB intensity, we plot the data from both [Fixsen et al. \(1998\)](#) and [Gispert et al. \(2000\)](#), while our best-fit model agrees better with [Gispert et al. \(2000\)](#). We note that the result from [Planck Collaboration XVIII \(2011, see their Figure 15\)](#) also agrees better with [Gispert et al. \(2000\)](#).

For the CFIRB power spectra, we demonstrate the contribution from the 2-halo term, 1-halo term, and the shot noise. For the angular scale measured by *Planck*, the 1-halo term is sub-dominant. In Figure B1, we can see that the agreement is good for almost all angular scales and all bands. The fit for the 217 GHz (1382 μm) auto-power spectrum is noticeably worse than other frequencies. We note that this band is dominated by the cosmic microwave background at all scales and has more uncertainties. For the 857 GHz (350 μm), the best-fit model slightly under-predicts the power at large angular scales (low ℓ).

4.4 Constraints on model parameters

In the following we discuss the implications of the constraints for each parameter. We quote the median and the 68% constraints for the 1-D marginalized posterior distribution.

- η_0 (minimum of the mass loading factor, which occurs at M_{pk}). The constraint is $0.44^{+0.03}_{-0.02}$. As mentioned in Section 2.3, several observations provided a lower limit for the mass loading factor but the observed values are inconclusive.
- α_1 (the slope of the mass loading factor at low-mass end): The constraint is $2.3^{+0.2}_{-0.2}$, which implies $\eta \propto M_{\text{h}}^{-2.3} \propto V_{\text{vir}}^{-7}$. This scaling is much steeper compared with any of the supernova wind models. Our model prefers a very low L_{IR} for low-mass haloes, which can be related to both low star formation rate and low-dust content. It has been shown that low-mass haloes tend to have a L_{IR} lower than expected from the SFR ([Hayward et al. 2014](#)), and the very steep α_1 can reflect both the low SFR and the low IR emission.
- α_2 (the slope of the mass loading factor at high-mass end): The constraint is $0.67^{+0.04}_{-0.04}$. As it is less than 1.1, the SFR does not decrease at the high-mass end (see Equation 4 and Figure 7). We will further discuss this trend at Section 6.1.
- β (slope of opacity, emissivity index): The constraint is $2.1^{+0.04}_{-0.03}$, which is close to the value $\beta = 2$ expected from theory ([Draine & Lee 1984](#)). It is higher than the results in [Planck Collaboration XXX \(2014, \$\beta=1.75\$ \)](#) and the nearby late-type galaxies observed by *Herschel* in [Boselli et al. \(2012, \$\beta=1.5\$ \)](#).
- σ (scatter of $\ln S_\nu$ and $\ln L_{\text{IR}}$ at a given halo mass): Our model indicates a rather large scatter, $0.88^{+0.05}_{-0.05}$ (0.27 dex), of L_{IR} and SFR at a given halo mass. This parameter is constrained by the shot noise; as we will see later, it also reproduces the bright-end of the IR luminosity functions (Figure 3). We note that such a large scatter is broadly consistent with our current knowledge of SFR. For example, the scatter between stellar mass and halo mass is estimated

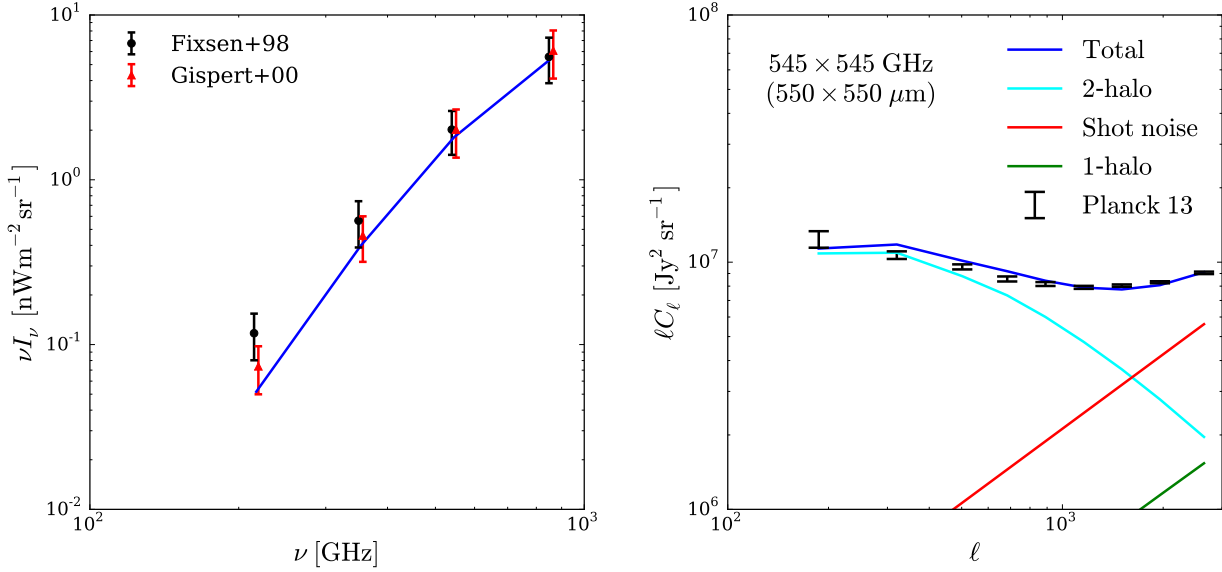


Figure 1. Joint model fit to CFIRB intensity and power spectra. **Left:** The CFIRB intensity measured by *COBE*-FIRAS (Fixsen et al. 1998; Gispert et al. 2000). We use the four frequencies associated with the *Planck*-HFI bands. The blue curve presents our best-fit model. **Right:** The CFIRB angular power spectra measured by Planck Collaboration XXX (2014). The blue curve is our model, which is broken down into the 2-halo term (cyan), the shot noise (red), and the 1-halo term (green). See Figure B1 for the auto and cross power spectra for 4 frequency bands.

to be 0.2 dex (e.g., Reddick et al. 2013), and the scatter between SFR and stellar mass is estimated to be 0.15 dex (e.g., Bernhard et al. 2014); summing these two scatter values in quadrature will lead to a scatter of 0.25 dex between SFR and halo mass.

- Extra redshift dependence (Equation 9): $z_0 = 0.68^{+0.04}_{-0.05}$; $\delta_1 = 2.2^{+0.2}_{-0.2}$; $\delta_2 = 1.1^{+0.06}_{-0.06}$. These values deviate from zero, indicating that the dark matter accretion rate (Equation 8) is insufficient to account for the full evolution of the SFR–mass relation.

- $f_{\text{ga}}p$ (product of f_{ga} and p , controlling the normalization of the $L_{\text{IR}}-M_{\text{h}}$ relation): The constraint is $0.57^{+0.03}_{-0.03}$, which is consistent with the value used in DM14 ($f_{\text{ga}} = 0.8$ and $p = 0.5$).

- yr (product of yield y and dust-to-metal ratio r): The constraint is $0.0033^{+0.0002}_{-0.0002}$. We note that Lilly et al. (2013) assumed $y = 0.016$, and Hayward et al. (2011) assumed $r = 0.4$. Our value is approximately half of the product of their values, which indicates either lower yield or lower dust-to-metal ratio.

- q (quenching factor for satellite galaxies): The constraint is $0.92^{+0.05}_{-0.05}$, indicating that satellite galaxies is not significantly fainter than central galaxies of the same halo mass.

- μ ($1-R$, R is the gas return fraction): The constraint is $0.61^{+0.04}_{-0.04}$, which is close to $\mu = 0.54$ estimated in Krumholz & Dekel (2012).

- $\log_{10} M_{\text{min}}$: The constraint is $10^{+0.6}_{-0.6}$. As the low-mass end of the luminosity-mass relation is very steep (α_1 is high), the power spectra are not sensitive to the value of $\log_{10} M_{\text{min}}$. In the halo model in Planck Collaboration XXX (2014), $\log_{10} M_{\text{min}}$ is similarly unconstrained.

- $\log_{10} M_{\text{pk}}$: The constraint is $12^{+0.04}_{-0.05}$. This is consistent

with our knowledge of the halo mass that has the highest star formation efficiency (Behroozi et al. 2013), but it is slightly lower than the constraints of the halo model in Planck Collaboration XXX (2014), $\log_{10} M_{\text{pk}} = 12.6 \pm 0.1$.

4.5 Summary of our model

Here we summarize the main scaling relations based on our parameter constraints. The L_{IR} -mass relations is given by

$$L_{\text{IR}}(M, z) = \frac{4.5 \times 10^{10}}{1 + 0.72f(M)} \left(\frac{M}{10^{12}} \right)^{1.1} g(z) L_{\odot}. \quad (33)$$

The dust mass is given by

$$M_{\text{d}}(M, z) = \frac{9 \times 10^6}{(1 + 0.72f(M))^2} \left(\frac{M}{10^{12}} \right)^{1.1} \left(\frac{t}{\text{Gyr}} \right) g(z) M_{\odot}, \quad (34)$$

and the dust temperature is given by

$$T_{\text{d}}(M, z) = 31 \left(\frac{1 + 0.72f(M)}{t/\text{Gyr}} \right)^{1/(4+\beta)} \text{K}. \quad (35)$$

In the equations above, the extra time dependence is given by

$$g(z) = (1 + 1.11z) \sqrt{\Omega_M(1+z)^3 + \Omega_{\Lambda}} \left(\frac{1+z}{1+0.68} \right)^{\delta}, \quad (36)$$

where $\delta = 2.2$ for $z \leq 0.68$, $\delta = 1.1$ for $z > 0.68$. The extra mass dependence is given by

$$f(M) = f(x, y) = 1 + x + y - (1 + x^{-1} + y^{-1})^{-1}, \quad (37)$$

where

$$x = \left(\frac{M}{10^{12}} \right)^{-2.3}, \quad y = \left(\frac{M}{10^{12}} \right)^{0.67}. \quad (38)$$

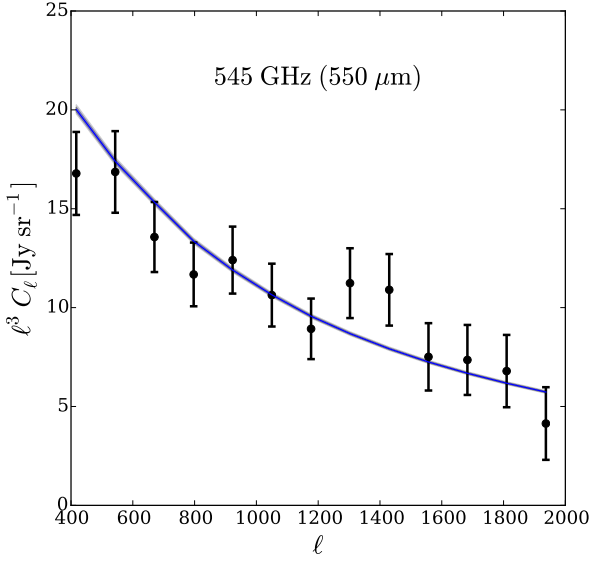


Figure 2. Correlation between CFIRB and CMB lensing potential. The blue band is the prediction from our model, while the data points are from [Planck Collaboration XVIII \(2014, see Figure B3 for all *Planck*-HFI bands\)](#).

In addition, t is the cosmic time

$$t = 14.6 \int_z^\infty \frac{dz'}{(1+z')\sqrt{\Omega_M(1+z')^3 + \Omega_\Lambda}} \text{ Gyr} . \quad (39)$$

Alternatively, one can use the fitting formula given in DM14, which is sufficiently accurate for $z > 1$,

$$t = 17.5(1+z)^{-1.5} \text{ Gyr} . \quad (40)$$

5 COMPARISONS WITH OTHER OBSERVATIONS

We now compare our model prediction with various other observations. We choose not to fit all observations simultaneously because of the different sources of systematic errors involved in them. In all the following calculations, we use 1% of our MCMC chains to calculate the model predictions, and we plot the median as well as the 68% and 95% intervals for all quantities. In the main text, we only show the results of a single band or redshift bin for demonstration; the full comparisons can be found in Appendix B.

5.1 Correlation between CFIRB and CMB lensing potential

[Planck Collaboration XVIII \(2014\)](#) presented the first detection of the correlation between CFIRB and CMB lensing potential. The CMB lensing potential is dominated by haloes at $1 \lesssim z \lesssim 3$ and is probed by the lower frequency bands of *Planck* (70 – 217 GHz), while the CFIRB redshift distribution peaks at $1 \lesssim z \lesssim 2$ and is measured by the higher frequency bands of *Planck*. Therefore, the correlation between the two provides a powerful probe for the connection

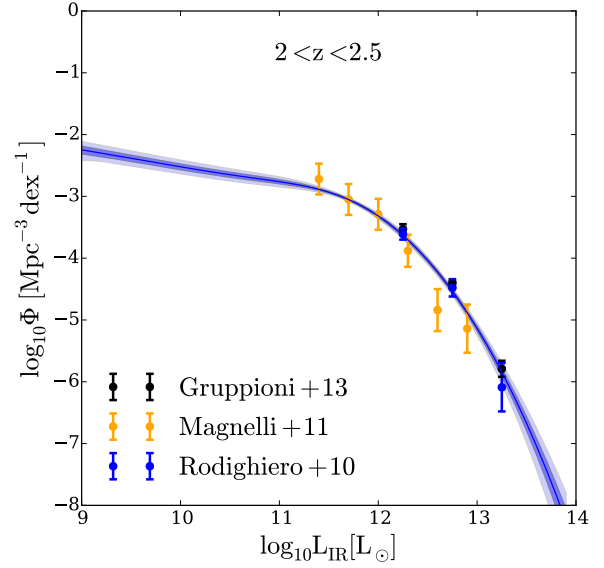


Figure 3. Bolometric infrared luminosity functions (8–1000 μm). The observational data sets include [Gruppioni et al. \(2013\)](#) from *Herschel*, as well as [Magnelli et al. \(2011\)](#) and [Rodighiero et al. \(2010\)](#) from *Spitzer* (see Figure B5 for multiple redshift bins between $z = 0$ and 4).

between dark matter and galaxies, as well as cross-check for systematics.

The cross power spectrum between the CMB lensing potential and CFIRB is given by

$$C_\ell^{\phi\nu} = \int_0^{\chi_*} B_\nu(z) \frac{3}{\ell^2} \Omega_M H_0^2 \left(\frac{\chi_* - \chi}{\chi_* \chi} \right) P_{\text{lin}} \left(k = \frac{\ell}{\chi}, z \right) d\chi , \quad (41)$$

where χ_* is the comoving distance to the last scattering surface, and $B_\nu(z)$ is given by Equation 23 and is equivalent to $b_{\text{eff}}(z)j_\nu(z)$.

Figures 2 and B3 show that our model can recover the measurements presented in [Planck Collaboration XVIII \(2014\)](#). We note that the 68% and 95% intervals are very small because our model is constrained by the CFIRB spectra, which have much smaller error bars. Assuming that the IR luminosity is independent of halo mass, [Planck Collaboration XVIII \(2014\)](#) applied a halo occupation distribution model and found that $\log_{10}(M_{\text{min}}/M_\odot) = 10.5 \pm 0.6$, where M_{min} is the minimum mass of a halo that hosts a central galaxy. [Planck Collaboration XVIII \(2014\)](#) interpreted this mass scale as the characteristic mass for haloes hosting CFIRB sources; however, as we will see below in Section 6.2 and Figure 8, the effective galaxy bias consistent with this data set (as well as the CFIRB auto-correlation) corresponds to a halo mass of $10^{12.5} M_\odot$ due to the mass dependence of star formation rate.

5.2 Bolometric infrared luminosity Functions

We assume that at a given M and z , the natural logarithm of the IR luminosity ($\ln L$) of galaxy follows a normal distri-

bution similar to $\ln S_\nu$,

$$P(\ln L|M) = \frac{1}{\sqrt{2\pi}\sigma} \exp \left[-\frac{(\ln L - \langle \ln L \rangle)^2}{2\sigma^2} \right]. \quad (42)$$

Here σ is the same as in Equation 27. We again ignore the contribution of satellite galaxies, and the luminosity function is given by

$$\frac{dn}{d\ln L}(z) = \int dM \frac{dn}{dM} P(\ln L|M). \quad (43)$$

We compare our model with the bolometric IR luminosity functions (integrating over 8–1000 μm) from the following publications:

- [Gruppioni et al. \(2013\)](#), Table 6 therein) based on *Herschel* (70–550 μm), $0 < z < 4.2$. The galaxies are selected from PACS (70, 100, 160 μm), and the SEDs are calibrated using SPIRE (250, 350, 550 μm).
- [Magnelli et al. \(2011\)](#), Table A6 therein) based on *Spitzer* (24 and 70 μm), $1.3 < z < 2.3$. They performed stacked analyses and derived the SED using the correlation between the luminosities at 24 and 70 μm .
- [Rodighiero et al. \(2010\)](#), Table 5 therein) based on *Spitzer* (8–24 μm), $0 < z < 2.5$. The SED was derived using luminosities from optical to 24 μm and was thus not probing the peak of the dust emission. Nevertheless, their results are consistent with the results from [Gruppioni et al. \(2013\)](#) based on longer wavelengths.
- [Le Floc'h et al. \(2005\)](#), Table 2 therein) based on *Spitzer* 8 μm , $0.3 < z < 1.2$. The bolometric luminosity was inferred from 24 μm .

Figure 3 shows the bolometric IR luminosity functions predicted from our model (see Figure B5 for 11 redshift bins up to $z = 4$). Since these data sets are based on slightly different redshift bins; we re-group these data points using the redshift bins in [Gruppioni et al. \(2013\)](#) and compute the model at the middle of the bin. We note that all these observations are based on mid-infrared and use various SED templates to calculate the bolometric IR luminosity; therefore, they can suffer from different statistical and systematic uncertainties and do not necessarily agree with other. Therefore, we also expect that they will not necessarily agree with our model constrained by CFIRB. As can be seen in Figure 3, our model agrees well with most of the data points. The scatter of the IR luminosity at a given mass (σ in Equation 27), as constrained by CFIRB, well captures the bright-end slopes of the IR luminosity functions.

5.3 Number counts of FIR galaxies

The number counts, also known as the flux density distribution function of infrared sources, is given by

$$\frac{dN}{dS_\nu}(z_1 < z < z_2) = \int_{z_1}^{z_2} dz \chi^2 \frac{d\chi}{dz} \frac{dn}{dS_\nu}. \quad (44)$$

We compare our model with the deep number counts measured by [Béthermin et al. \(2012\)](#) in the HerMES program. These authors used the maps in 250, 350, and 500 μm in the COSMOS and GOODS-N field observed by *Herschel*-SPIRE, and they used the catalogs of *Spitzer* 24 μm as priors for positions, flux densities, and redshifts. They provided the

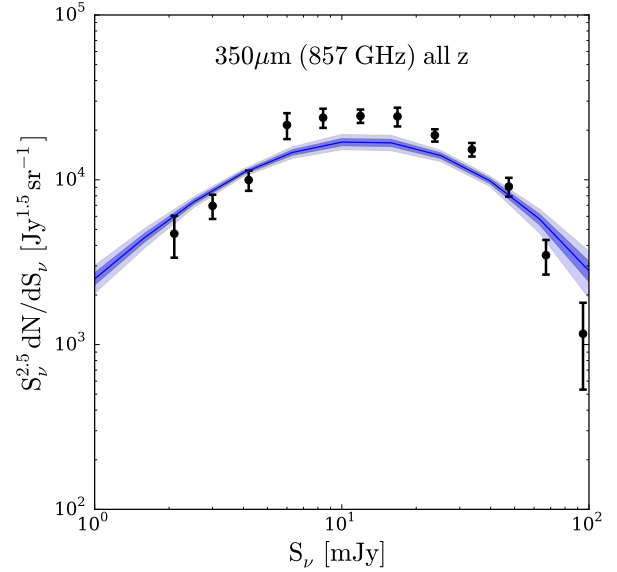


Figure 4. Number counts of infrared galaxies. The data points are from [Béthermin et al. \(2012\)](#) based on *Herschel*-SPIRE. Our model can recover the total number counts in the three bands, while it under-predicts the source counts for $z < 1$ (see Figure B6 for all *Herschel*-SPIRE bands and several redshift bins).

resolved number counts for > 20 mJy and stacked number counts for between 2 to 20 mJy for several redshift bins.

Figure 4 shows the comparison between our model (blue band) with the data points from [Béthermin et al. \(2012\)](#); the full comparison is presented in Figure B6. As can be seen, our model agrees with the total number counts from all redshifts (the first row). We note that our model does not include the strongly lensed galaxies, which can contribute significantly to the bright end of the number counts functions.

On the other hand, when we compare with individual redshift bins in [Béthermin et al. \(2012\)](#), our model tend to produce lower number counts for $z < 1$ and higher number counts for $z > 2$. This is discrepancy is puzzling because our model agrees well with the evolution of IR luminosity function (Figure B5), as well as the cosmic star formation history discussed below (Figure 9).

5.4 Redshift distribution of CFIRB

The redshift distribution of CFIRB emission is given by

$$\frac{dI_\nu}{dz} = \chi^2 \frac{d\chi}{dz} \int dS_\nu \frac{dn}{dS_\nu} S_\nu \quad (45)$$

We again compare our model with the data set from [Béthermin et al. \(2012\)](#), which was discussed in the previous section.

Independently, [Viero et al. \(2013b\)](#) conducted a stacking analysis to quantify the fraction of CFIRB from galaxies resolved in optical/NIR. Specifically, they used the optical galaxy catalog from the Ultra-Deep Survey fields from the UKIRT Infrared Deep Survey. Using the galaxy positions and photometric redshift, they performed stacking analyses

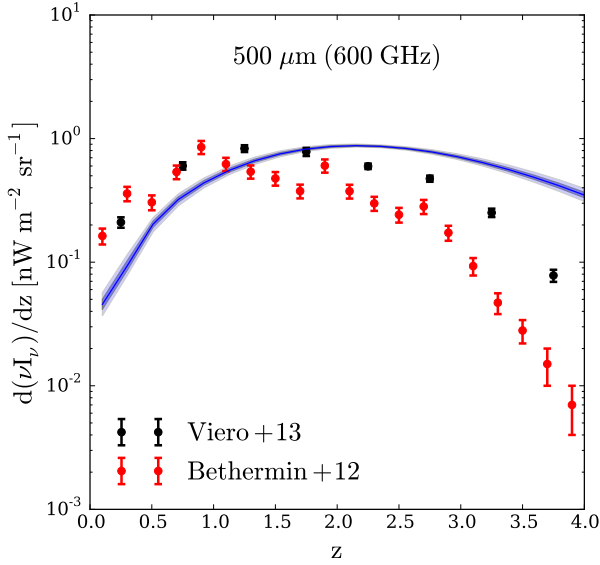


Figure 5. Redshift distribution of CFIRB emission. The data points are from *resolved* sources in Viero et al. (2013b, black points, based on optical/NIR) and Béthermin et al. (2012, red points, based on 24 μm), which serve as lower limits. Our model is above the data points for $z > 1.5$ but is slightly lower for $z < 1$ (see Figure B4 for all bands of *Herschel*-SPIRE).

on FIR maps, including the 250, 350, and 500 μm data from *Herschel*-SPIRE, and the 1100 μm data from AzTEC. With this analysis, they were able to separate the contribution of CFIRB from star-forming and quiescent galaxies in different stellar mass and redshift ranges. Their sample resolves 80%, 69%, 65%, and 45% of CFIRB in 250, 350, 500, and 1100 μm , respectively. As mentioned in Viero et al. (2013b), these measurements should be considered as lower limits, since optical catalogs can miss galaxies in FIR, either due to heavy dust obscuration or low intrinsic luminosity. The completeness also decreases rapidly with redshift. Viero et al. (2013b) also suggested that such measurements provide an effective way to break the degeneracies between redshift distribution, temperature, and halo bias.

Figure 5 presents the comparison between the redshift distribution of CFIRB from our model (blue band) and the results in Béthermin et al. (2012, red points) and Viero et al. (2013b, black points). Our model predicts higher differential intensity for $z > 1.5$ than the data points, which should be considered as lower limits. If we use a lower differential intensity that is consistent with the data points, we will underestimate the total CFIRB intensity and clustering. On the other hand, our model predicts slightly lower differential intensity for $z < 1$. This is consistent with what we saw in Figure 4, where our model also under-predicts the number counts for $z < 1$ observed by *Herschel*.

5.5 CFIRB power spectrum from *Herschel*

Figure 6 shows the CFIRB power spectrum at 350 μm measured by *Herschel* (Viero et al. 2013a), compared with our

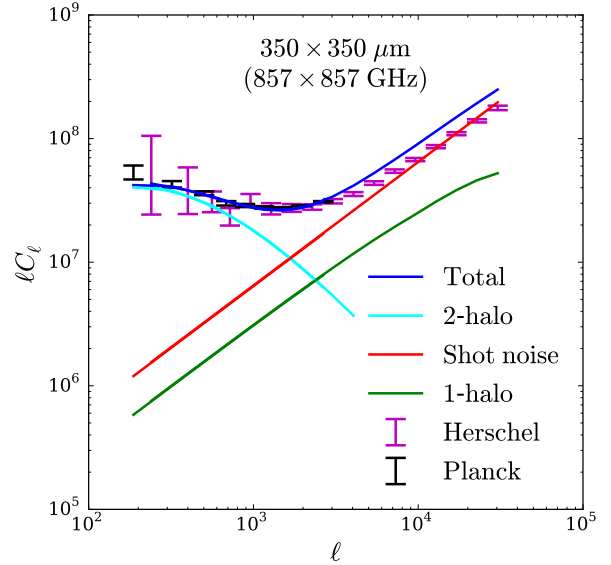


Figure 6. Comparison between our model and the power spectra from *Herschel* published in Viero et al. (2013a). Our model constrained by *Planck* overproduces the small-scale power when compared with *Herschel*. We show the power spectra of both *Planck* and *Herschel* in their common frequency 857 GHz (350 μm) to illustrate the different angular scale and sizes of error bars (see Figure B2 for all frequencies for *Herschel*-SPIRE).

model and the measurement of *Planck* in the same band. Figure B2 shows the comparison between our model and all frequencies of *Herschel*-SPIRE. The power spectra are based on the HerMES program, which covers 70 deg^2 in 250, 350, and 500 μm . The galactic cirrus was removed using the 100 μm maps from IRAS. Compared with the *Planck* data, the *Herschel* power spectra extend to smaller angular scales.

As can be seen, our model over-predict the power for $\ell \gtrsim 4000$. The sum of the shot noise (red) and the 1-halo term (green) exceeds the data points. That is, the *Planck* power spectra favor higher clustering at small scales. We have tried to jointly fit the *Planck* and *Herschel* spectra, but such jointly-constrained models under-predict the high- ℓ power in *Planck* and also under-predict the cosmic star formation rate density (see Section 6.3 and Figure 9 below). Since our model agrees well (even slightly underestimates) the total number counts of FIR sources measured from *Herschel* (see Figure 4), it indicates inconsistencies between the number counts and shot noise. We note that such inconsistencies have also been observed in the analyses by the *Herschel* team (P. Serra, private communications).

6 IMPLICATIONS OF OUR MODEL

Based on the constraints on parameters, we calculate various properties of dusty star-forming galaxies and compare them with observations.

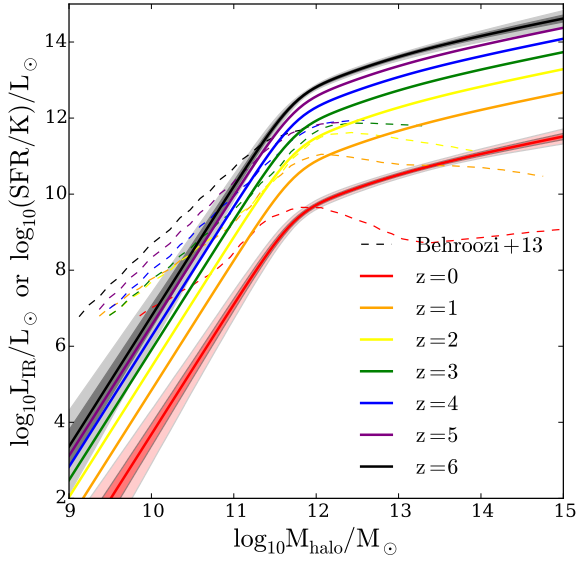


Figure 7. Infrared luminosity vs. halo mass in our model (solid curves); the function is provided in Equation 33. Comparing with the SFR constraints from UV/optical/NIR from Behroozi et al. (2013, dash curves) and assuming $L_{\text{IR}} = \text{SFR}/K$, we find that the L_{IR} at low-mass end is lower than expected from SFR, while the high-mass end requires higher L_{IR} than expected from SFR.

6.1 IR luminosity–mass relation

Figure 7 shows the mean relation between the infrared luminosity and the halo mass constrained by CFIRB (Equations 33). The solid curves correspond to our model at various redshifts. The dash curves show the $L_{\text{IR}}-M_{\text{h}}$ relation expected from the SFR from Behroozi et al. (2013) and $L_{\text{IR}} = \text{SFR}/K$.

For low-mass haloes, L_{IR} is lower than the expectation from SFR. These low-mass haloes tend to have low dust mass and thus lower IR luminosity given their SFR. For example, using hydrodynamic simulations with radiative transfer, Hayward et al. (2014) have shown that low-mass galaxies are inefficient in absorbing UV photons, and inferring SFR from the IR luminosity can significantly underestimate the SFR for these galaxies (also see, e.g., Jonsson et al. 2006). Using the data from HerMES, Heinis et al. (2014) have found that galaxies with low stellar mass have lower dust attenuation, as well as lower IR excess (the ratio between L_{IR} and L_{UV}); this confirms the findings in simulations that low-mass galaxies are inefficient in absorbing UV photons. In principle, when converting SFR to L_{IR} , one should consider the mass dependence of dust attenuation. We will explore this in future work.

For massive haloes, the IR luminosity is significantly higher than what we expected from star formation rate. The CFIRB power spectra indicate a rather high galaxy bias that requires the contribution of FIR photons from massive haloes (see Section 6.2 below). If we use the $L_{\text{IR}}-M_{\text{h}}$ relation from Behroozi et al. (2013) in our halo model to calculate the power spectra, the amplitude of the CFIRB power spectra are too low regardless of the dust temperature used.

We note that, in addition to massive young stars, old stars can also heat the dust and contribute to FIR emission (e.g., Groves et al. 2012; Fumagalli et al. 2014; Utomo et al. 2014). For example, using hydrodynamic simulations with radiative transfer, Narayanan et al. (2015) have found that old stars can contribute to up to half of the IR luminosity. In addition, the heating from old stars contributes to a larger fraction of the IR luminosity for quiescent galaxies than for star-forming galaxies (e.g., Fumagalli et al. 2014). Since these massive haloes tend to host quiescent galaxies, we expect that the contribution of heating of old stars is significant.

On the other hand, dust-obscured AGN can also heat the dust and contribute the FIR emissions (e.g., Alexander et al. 2005; Lutz et al. 2005; Yan et al. 2005; Le Floc’h et al. 2007; Sajina et al. 2012; Dai et al. 2015). However, the contribution from AGNs are expected to be low for massive galaxies; it has been shown that luminous AGNs are hosted by haloes of mass $10^{12} - 10^{13} M_{\odot}$ (e.g., Alexander & Hickox 2012). Therefore, AGNs are unlikely to be the main sources of the excess FIR emission.

The excess of FIR light for massive haloes has also been seen in previous publications. For example, Clements et al. (2014) matched *Planck* sources and HerMES survey from *Herschel* and found 4 clumps consistent with galaxy clusters at $0.8 < z < 2.3$. They found that these cluster-like clumps have $L_{\text{IR}} = 3 - 70 \times 10^{12} L_{\odot}$; if one assumes that all the IR emissions are associated with star formation, such IR luminosities would imply a star formation rate of $600 - 10^4 M_{\odot} \text{yr}^{-1}$. Narayanan et al. (2015) used hydrodynamic simulations with radiative transfer to show that at $z \approx 2 - 3$, a dark matter halo of $10^{13} M_{\odot}$ can have very high star formation rate ($500 - 1000 M_{\odot} \text{yr}^{-1}$). Such haloes can host groups of galaxies that are bright in submm for a prolonged period due to constant gas infall. These findings suggest that there can indeed be IR-bright galaxies in massive haloes, which contribute the strong galaxy bias we find for CFIRB.

6.2 Effective bias

Figure 8 shows the large-scale effective bias calculated from our model,

$$b_{\text{eff}} = \frac{B_{\nu}(z)}{j_{\nu}(z)}, \quad (46)$$

where $B_{\nu}(z)$ and $j_{\nu}(z)$ are given by Equations 18 and 23. We note that since the SED depends on halo mass, the effective bias weakly depends on the frequency. For comparison, we show the bias of haloes of $M_{\text{h}} = 10^{12, 12.5, 13} M_{\odot}$ as a function of redshift, using the fitting function from Tinker et al. (2010). As can be seen, our effective bias is consistent with haloes of mass $10^{13} M_{\odot}$ at $z = 0$ and $10^{12.5} M_{\odot}$ at $z = 2$. The CFIRB data favors a high galaxy bias and thus higher L_{IR} for massive haloes.

An alternative explanation of this high galaxy bias could be that FIR galaxies represent biased environments, and the simple linear halo bias does not apply. It has been shown that the halo bias, in addition to its dependence on halo mass, can depend on formation time, concentration, and occupation (e.g. Wechsler et al. 2006). If FIR galaxies preferentially reside in haloes with recent major merger, or

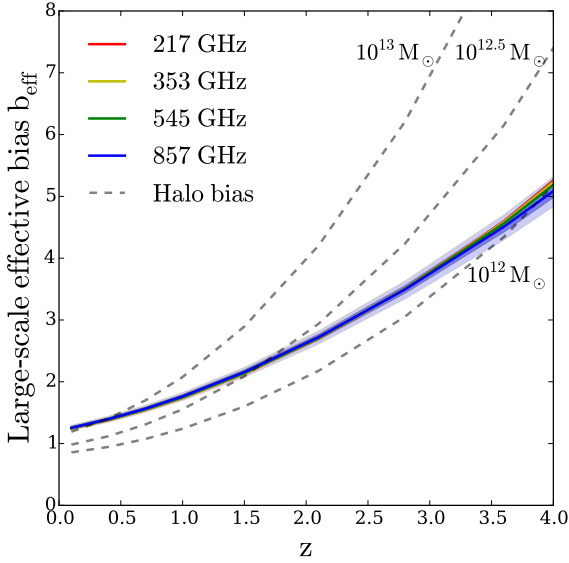


Figure 8. The effective bias from our model, which is consistent with halo mass $10^{13}M_{\odot}$ at $z = 0$ and $10^{12.5}M_{\odot}$ at $z = 2$.

if the FIR luminosity and formation history are correlated, it might be possible to explain the high galaxy bias without invoking extra FIR sources in massive haloes. We will explore this in future work.

6.3 Global star formation rate density

Figure 9 shows the star formation rate density based on our model,

$$\rho_{\text{SFR}}(z) = K \int dM \frac{dn}{dM} L_{\text{IR}}(M, z), \quad (47)$$

where K is $1.7 \times 10^{-10} M_{\odot} \text{yr}^{-1} L_{\odot}^{-1}$ (Kennicutt 1998, assuming Salpeter initial mass function).

We fit the four-parameter function proposed in Madau & Dickinson (2014) to our ρ_{SFR} (also see Robertson et al. 2015)

$$\rho_{\text{SFR}}(z) = a_p \frac{(1+z)^{b_p}}{1 + [(1+z)/c_p]^{d_p}} M_{\odot} \text{Mpc}^{-3} \text{yr}^{-1} \quad (48)$$

where

$$\begin{aligned} a_p &= 0.0082^{+0.0005}_{-0.0004} \\ b_p &= 3^{+0.1}_{-0.1} \\ c_p &= 3.4^{+0.1}_{-0.1} \\ d_p &= 5.5^{+0.2}_{-0.2}. \end{aligned} \quad (49)$$

We note that these parameters are highly degenerate with each other.

For comparison, we plot the results based on UV and IR luminosity functions compiled by Madau & Dickinson (2014, Table 1 and references therein). The green points correspond to the results from FUV luminosity function (1500Å) from *GALEX* and *HST* with corrections of dust attenuation. The red points correspond to the results from the IR luminosity

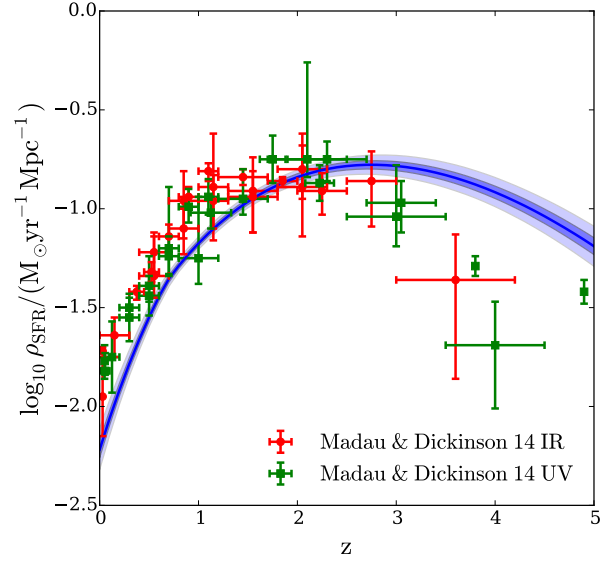


Figure 9. Cosmic star formation rate density inferred from our model (blue band). Our model is consistent with the results from Madau & Dickinson (2014, red and green points).

function (8–1000μm) from *IRAS*, *Spitzer*, and *Herschel*. We note that Madau & Dickinson (2014) re-computed the total luminosity density by extrapolating the best-fit luminosity functions down to $0.03L_*$ at each redshift from each publication. The faint-end slope and the dust extinction can therefore lead to significant uncertainties. They also cautioned that there is no robust measurements of star formation rate density for $z \gg 2$ due to the lack of robust selections. We also note that Robertson et al. (2015) found results very similar to Madau & Dickinson (2014) when they added a few more UV results, extrapolated the observed UV and IR luminosity functions down to lower luminosities, and included the constraints of the integrated Thompson optical depth from Planck Collaboration XVI (2014).

Overall, our model agrees with constraints from Madau & Dickinson (2014). For $z < 1$, our SFR is slightly lower, which corresponds to the fact that L_{IR} can underestimate SFR for low-mass galaxies, as discussed in Section 6.1 and shown in Figure 7. For high redshift ($z > 3$), CFIRB does not provide strong constraints on the SFR, and the result is extrapolation from low redshift; however, it is marginally consistent with UV constraints. We note that the halo model in Planck Collaboration XXX (2014) gave very high SFR density at high redshift, which could be related to their parameterization of redshift evolution.

6.4 Cosmic dust mass density

Figure 10 shows the cosmic dust mass density calculated from our model. The dust density is calculated by integrating over the halo mass function in physical units,

$$\rho_{\text{dust}}(z) = \int dz \frac{dn}{dM} M_{\text{dust}}(M, z). \quad (50)$$

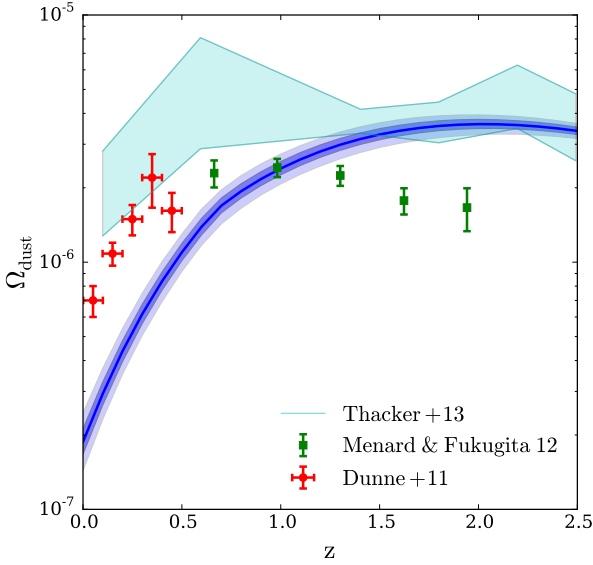


Figure 10. Cosmic dust mass density inferred from our model. Compared with the results from Thacker et al. (2013) using CFIRB of H-ATLAS and from Dunne et al. (2011) using the luminosity functions of H-ATLAS, our results are consistent at $z > 1$ but are lower at $z < 1$. We note that the results from Ménard & Fukugita (2012) using Mg II absorbers serve as a lower limit of the dust in galactic haloes.

We express the dust mass density in unit of the critical density of the Universe,

$$\Omega_{\text{dust}}(z) = \frac{\rho_{\text{dust}}(z)}{\rho_{\text{crit}}(z)}, \quad (51)$$

where

$$\rho_{\text{crit}}(z) = 2.775 \times 10^{11} h^2 \left(\Omega_M (1+z)^3 + \Omega_\Lambda \right) \text{M}_\odot \text{Mpc}^{-3}. \quad (52)$$

For $z > 1$, our results are consistent with the results of Thacker et al. (2013) based on the CFIRB power spectra from H-ATLAS of *Herschel*. For $z < 1$, our results are lower than Thacker et al. (2013) and the low-redshift results of Dunne et al. (2011), which were derived from the luminosity functions of H-ATLAS. This is related to the fact that our model predicts lower number counts than those observed by *Herschel*. For comparison, we include the results using Mg II absorber from Ménard & Fukugita (2012). The dust mass density derived from Mg II serves as a lower limit for the dust associated with galactic haloes; the dust associated with galactic discs has been shown to be comparable to the dust associated with galactic haloes (Fukugita & Peebles 2004; Driver et al. 2007). Therefore, the total dust mass associated with galaxies is approximately twice of the values of the data points of Ménard & Fukugita (2012).

6.5 Dust temperature and mass

Figure 11 shows the dust properties from our model. The left/right panel corresponds to dust temperature/mass vs. IR luminosity at various redshifts, shown by different colors.

Our model predicts a non-monotonic relations with L_{IR} ; M_d tends to be low at both the bright and faint ends, while T_d tends to be high at both ends. This can be understood through the mass dependence of the mass loading factor. In our model, the dust mass is given by

$$M_d \propto \frac{1}{(1 - R + \eta)^2} \quad (53)$$

(see Equations 12 and 34). The high mass loading factor for both high- and low-mass haloes leads to strong mass outflow and thus low dust mass. In addition, under the assumption of local thermal equilibrium, the dust temperature depends on the ratio between L_{IR} and M_d ,

$$T_d \propto \left(\frac{L_{\text{IR}}}{M_d} \right)^{1/(4+\beta)} \propto (1 - R + \eta)^{1/(4+\beta)} \quad (54)$$

(see Equations 15 and 35). Therefore, at a given redshift, haloes at both high- and low-mass ends tend to have high dust temperature due to the high mass loading factor.

We compare our results with the observational results in Magnelli et al. (2012, M12 thereafter), which include 61 submm galaxies (SMG) selected from ground-based observations and observed with PACS and SPIRE instruments onboard *Herschel*. We caution that this comparison is mainly for demonstrating the range of values rather than constraining the model, as the observations of SMG tend to select merger-driven starbursts and has incomplete coverage for the main-sequence galaxies. As stated in M12, for high IR luminosity, the sample is representative of the entire SMG population, but these galaxies tend to be associated with merger-driven starbursts; on the other hand, for low IR luminosity, the sample tends biased toward low redshift and colder dust. M12 concluded that approximately half of the sample is consistent with the merger-drive starbursts, while the other half is consistent with the main sequence of stellar mass and SFR. That is, this sample may not be relevant for the galaxies contributing to the CFIRB.

The left panel of Figure 11 shows the relation between T_d and L_{IR} predicted from our model. The correlation between L_{IR} and T_d has been known for SMG (Chapman et al. 2005; Hwang et al. 2010; Hayward et al. 2012). In M12, T_d and L_{IR} are derived from fitting the SED to a modified blackbody with a single dust temperature, with $\beta = 1.5$. We note that M12 used 40–120 μm to calculate L_{FIR} and assumed $L_{\text{IR}} = 1.91 L_{\text{FIR}}$. The dust temperature from M12 is slightly lower than ours for $z < 2$. This may reflect the SMG selection tends to bias towards low-redshift, low-temperature galaxies. In our model, the trend is reversed for faint galaxies; since we require strong feedback to suppress the star formation rate for low-mass haloes, this feedback also suppresses the dust mass and increases the dust temperature.

The right panel of Figure 11 shows the relation between M_d and L_{IR} from our model, as well as the measurements in M12. To derive the dust mass, M12 assumed a power-law distribution of dust temperature and fit the SED. Our model is consistent with M12. Nevertheless, M12 shows higher dust mass for $z < 2$, and this difference is related to the lower dust temperature seen in the left panel.

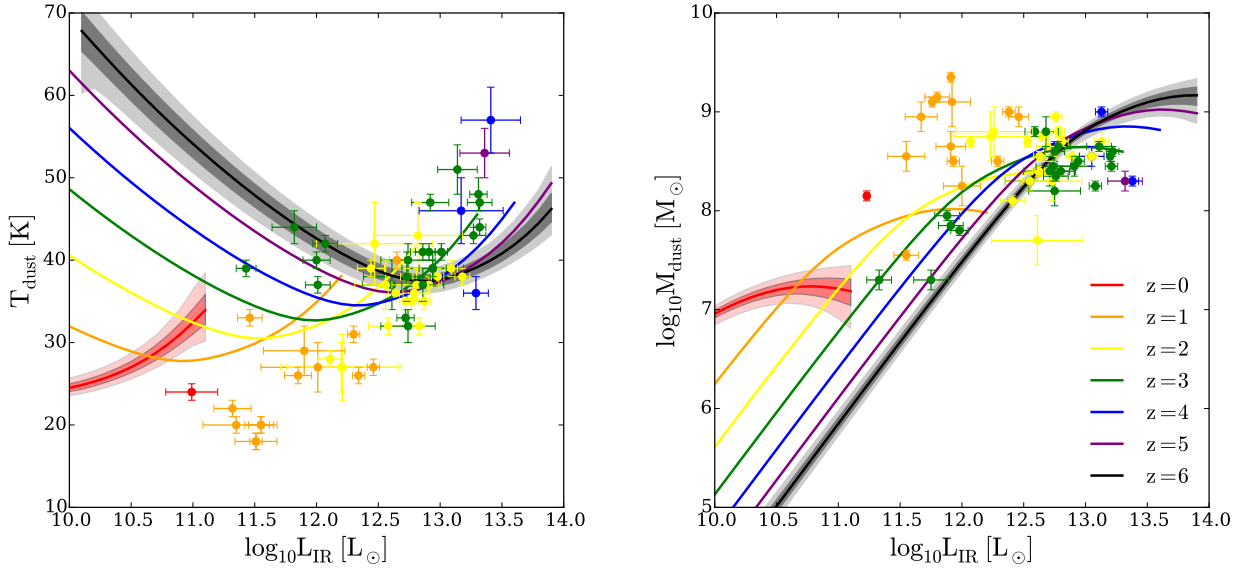


Figure 11. Dust properties from our model compared with observations of 61 submm galaxies observed by *Herschel* (Magnelli et al. 2012). We note that this figure is mainly for demonstrating the orders of magnitude because of the complex selection function involved. **Left:** Our model predicts higher dust temperature than the observation. **Right:** Our mean dust mass is slightly lower than the observation.

7 SUMMARY

We apply the gas regulator model of galaxy evolution to describe dusty star-forming galaxies across cosmic time. We fit the model to the CFIRB power spectra observed by *Planck* and the total intensity measured by *COBE*. The model successfully predicts the correlation between CFIRB and CMB lensing potential measured by *Planck*, the bolometric IR luminosity functions up to $z = 4$ from *Herschel* and *Spitzer*, and the total number counts from *Herschel*. However, our model under-predicts the number counts of *Herschel* for $z < 1$, slightly under-predicts the differential CFIRB intensity of *Herschel* for $z < 1$, and slightly over-predicts the CFIRB power spectra of *Herschel* at small scales.

The implications of our model are summarized as follows:

- The CFIRB power spectra favor a strong clustering of FIR galaxies. At $z = 0$ ($z = 2$), the large-scale galaxy bias is equivalent to the bias of dark matter haloes of mass 10^{13} ($10^{12.5}$) M_{\odot} . This galaxy bias is consistent with the correlation between CFIRB and CMB lensing potential.
- The luminosity–mass relation from our model indicates that for massive haloes, the IR luminosity is higher than expected from the star formation rate constrained by UV, optical, and NIR. This result is consistent with the high galaxy bias we have found. This excess in IR luminosity for massive haloes may come from dust heated by old stellar populations, obscured active galactic nuclei, or obscured major mergers.
- In our model, the luminosity–mass relation for low-mass haloes is lower than expected from the star formation rate. These low-mass galaxies tend to be inefficient in absorbing UV photons, and their FIR emissions can underestimate the true SFR.
- The cosmic star formation history from our model

agrees with the recent compilation of Madau & Dickinson (2014). In addition, the total dust mass density across cosmic time is consistent with the results from *Herschel* CFIRB at $z > 1$, while it is lower than the results from IR luminosity functions at $z < 1$.

- Compared with submm galaxies selected from ground-based surveys, the galaxies in our model tend to have higher dust temperature ($T_{\text{dust}} \gtrsim 25$ at $z = 0$ and increases with redshift) and lower dust mass.

Our theoretical framework provides a simple, physically-motivated way to compare different FIR observations. It can easily be generalized to compute the foreground for various intensity mapping experiments. Our framework will also be useful for optimizing the survey designs and strategies for future FIR surveys. For example, the next generation CMB experiments, such as PIXIE (Kogut et al. 2011) and COrE (The COrE Collaboration et al. 2011), will provide larger frequency coverage and/or higher angular resolution than *Planck* and will be able to provide better measurements for the CFIRB anisotropies as well as individual sources. The Far-IR Surveyor, which is currently explored by NASA³, will reveal many more properties of dusty star-forming galaxies.

ACKNOWLEDGEMENTS

We thank Chris Hayward, Lorenzo Monceli, Paolo Serra, Jason Sun, and Marco Viero for helpful discussions. H.W. acknowledges the support by the U.S. National Science Foundation grant AST1313037. The calculations in this work were performed on the Zwicky cluster of Caltech Center for

³ <http://asd.gsfc.nasa.gov/firs/>

Advanced Computing Research and on the Piz Dora cluster of the Swiss National Supercomputing Centre. Part of the research described in this paper was carried out at the Jet Propulsion Laboratory, California Institute of Technology, under a contract with the National Aeronautics and Space Administration.

REFERENCES

- Addison G. E., Dunkley J., Bond J. R., 2013, *MNRAS*, **436**, 1896
- Alexander D. M., Hickox R. C., 2012, *New Astronomy Reviews*, **56**, 93
- Alexander D. M., Bauer F. E., Chapman S. C., Smail I., Blain A. W., Brandt W. N., Ivison R. J., 2005, *ApJ*, **632**, 736
- Amblard A., Cooray A., Serra P., et al., 2011, *Nature*, **470**, 510
- Behroozi P. S., Wechsler R. H., Conroy C., 2013, *ApJ*, **770**, 57
- Benson A. J., 2010, *Phys. Rep.*, **495**, 33
- Benson A. J., Bower R. G., Frenk C. S., Lacey C. G., Baugh C. M., Cole S., 2003, *ApJ*, **599**, 38
- Bernhard E., Béthermin M., Sargent M., Buat V., Mullaney J. R., Pannella M., Heinis S., Daddi E., 2014, *MNRAS*, **442**, 509
- Berta S., Magnelli B., Nordon R., et al., 2011, *A&A*, **532**, A49
- Béthermin M., Le Floc'h E., Ilbert O., et al., 2012, *A&A*, **542**, A58
- Béthermin M., Wang L., Doré O., Lagache G., Sargent M., Daddi E., Cousin M., Aussel H., 2013, *A&A*, **557**, A66
- Bond J. R., Carr B. J., Hogan C. J., 1986, *ApJ*, **306**, 428
- Boselli A., Ciesla L., Cortese L., et al., 2012, *A&A*, **540**, A54
- Bouché N., et al., 2010, *ApJ*, **718**, 1001
- Chapman S. C., Blain A. W., Smail I., Ivison R. J., 2005, *ApJ*, **622**, 772
- Chen Y.-M., Tremonti C. A., Heckman T. M., Kauffmann G., Weiner B. J., Brinchmann J., Wang J., 2010, *AJ*, **140**, 445
- Clements D. L., Braglia F. G., Hyde A. K., et al., 2014, *MNRAS*, **439**, 1193
- Cooray A., Sheth R., 2002, *Phys. Rep.*, **372**, 1
- Croton D. J., et al., 2006, *MNRAS*, **365**, 11
- Dai Y. S., Wilkes B. J., Bergeron J., Omont A., Kuraszewicz J., Teplitz H. I., 2015, ArXiv:1511.06761,
- De Bernardis F., Cooray A., 2012, *ApJ*, **760**, 14
- Dekel A., Mandelker N., 2014, *MNRAS*, **444**, 2071
- Dekel A., Zlotov A., Tweed D., Cacciato M., Ceverino D., Primack J. R., 2013, *MNRAS*, **435**, 999
- Dole H., et al., 2006, *A&A*, **451**, 417
- Draine B. T., Lee H. M., 1984, *ApJ*, **285**, 89
- Driver S. P., Popescu C. C., Tuffs R. J., Liske J., Graham A. W., Allen P. D., de Propris R., 2007, *MNRAS*, **379**, 1022
- Dunne L., Gomez H. L., da Cunha E., et al., 2011, *MNRAS*, **417**, 1510
- Dutton A. A., van den Bosch F. C., 2009, *MNRAS*, **396**, 141
- Elbaz D., Cesarsky C. J., Chanial P., Aussel H., Franceschini A., Fadda D., Chary R. R., 2002, *A&A*, **384**, 848
- Erb D. K., 2015, *Nature*, **523**, 169
- Fakhouri O., Ma C.-P., Boylan-Kolchin M., 2010, *MNRAS*, **406**, 2267
- Feldmann R., 2015, *MNRAS*, **449**, 3274
- Fixsen D. J., Dwek E., Mather J. C., Bennett C. L., Shafer R. A., 1998, *ApJ*, **508**, 123
- Foreman-Mackey D., Hogg D. W., Lang D., Goodman J., 2013, *PASP*, **125**, 306
- Fukugita M., Peebles P. J. E., 2004, *ApJ*, **616**, 643
- Fumagalli M., Labbé I., Patel S. G., et al., 2014, *ApJ*, **796**, 35
- Gelman A., Rubin D. B., 1992, *Statistical Science*, **7**, 457
- Gispert R., Lagache G., Puget J. L., 2000, *A&A*, **360**, 1
- Grossan B., Smoot G. F., 2007, *A&A*, **474**, 731
- Groves B., et al., 2012, *MNRAS*, **426**, 892
- Gruppioni C., et al., 2013, *MNRAS*, **432**, 23
- Guo Q., et al., 2011, *MNRAS*, **413**, 101
- Hajian A., Viero M. P., Addison G., et al., 2012, *ApJ*, **744**, 40
- Hall N. R., Keisler R., Knox L., et al., 2010, *ApJ*, **718**, 632
- Hauser M. G., Dwek E., 2001, *ARA&A*, **39**, 249
- Hauser M. G., Arendt R. G., Kelsall T., et al., 1998, *ApJ*, **508**, 25
- Hayward C. C., Hopkins P. F., 2015, arXiv:1510.05650,
- Hayward C. C., Kereš D., Jonsson P., Narayanan D., Cox T. J., Hernquist L., 2011, *ApJ*, **743**, 159
- Hayward C. C., Jonsson P., Kereš D., Magnelli B., Hernquist L., Cox T. J., 2012, *MNRAS*, **424**, 951
- Hayward C. C., et al., 2014, *MNRAS*, **445**, 1598
- Heinis S., Buat V., Béthermin M., et al., 2014, *MNRAS*, **437**, 1268
- Hopkins P. F., Quataert E., Murray N., 2012, *MNRAS*, **421**, 3522
- Hwang H. S., Elbaz D., Magdis G., et al., 2010, *MNRAS*, **409**, 75
- Jonsson P., Cox T. J., Primack J. R., Somerville R. S., 2006, *ApJ*, **637**, 255
- Kennicutt Jr. R. C., 1998, *ApJ*, **498**, 541
- Kogut A., Fixsen D. J., Chuss D. T., et al., 2011, *J. Cosmol. Astropart. Phys.*, **7**, 25
- Krumholz M. R., Dekel A., 2012, *ApJ*, **753**, 16
- Lagache G., Puget J. L., 2000, *A&A*, **355**, 17
- Lagache G., Bavouzet N., Fernandez-Conde N., Ponthieu N., Rodet T., Dole H., Miville-Deschênes M.-A., Puget J.-L., 2007, *ApJ*, **665**, L89
- Le Floc'h E., Papovich C., Dole H., et al., 2005, *ApJ*, **632**, 169
- Le Floc'h E., Willmer C. N. A., Noeske K., et al., 2007, *ApJ*, **660**, L65
- Lewis A., Challinor A., Lasenby A., 2000, *ApJ*, **538**, 473
- Lilly S. J., Carollo C. M., Pipino A., Renzini A., Peng Y., 2013, *ApJ*, **772**, 119
- Lu Y., Blanc G. A., Benson A., 2015, *ApJ*, **808**, 129
- Lutz D., Valiante E., Sturm E., et al., 2005, *ApJ*, **625**, L83
- Lutz D., Mainieri V., Rafferty D., et al., 2010, *ApJ*, **712**, 1287
- Madau P., Dickinson M., 2014, *ARA&A*, **52**, 415
- Magnelli B., Elbaz D., Chary R. R., Dickinson M., Le Borgne D., Frayer D. T., Willmer C. N. A., 2011, *A&A*, **528**, A35
- Magnelli B., Lutz D., Santini P., et al., 2012, *A&A*, **539**, A155
- Martin C. L., Shapley A. E., Coil A. L., Kornei K. A., Bundy K., Weiner B. J., Noeske K. G., Schiminovich D., 2012, *ApJ*, **760**, 127
- Matsuhara H., Kawara K., Sato Y., et al., 2000, *A&A*, **361**, 407
- Ménard B., Fukugita M., 2012, *ApJ*, **754**, 116
- Muratov A. L., Kereš D., Faucher-Giguère C.-A., Hopkins P. F., Quataert E., Murray N., 2015, *MNRAS*, **454**, 2691
- Murray N., Quataert E., Thompson T. A., 2005, *ApJ*, **618**, 569
- Narayanan D., Turk M., Feldmann R., et al., 2015, *Nature*, **525**, 496
- Navarro J. F., Frenk C. S., White S. D. M., 1997, *ApJ*, **490**, 493
- Partridge R. B., Peebles P. J. E., 1967, *ApJ*, **148**, 377
- Planck Collaboration XVI 2014, *A&A*, **571**, A16
- Planck Collaboration XVIII 2011, *A&A*, **536**, A18
- Planck Collaboration XVIII 2014, *A&A*, **571**, A18
- Planck Collaboration XXX 2014, *A&A*, **571**, A30
- Puget J.-L., Abergel A., Bernard J.-P., Boulanger F., Burton W. B., Desert F.-X., Hartmann D., 1996, *A&A*, **308**, L5
- Reddick R. M., Wechsler R. H., Tinker J. L., Behroozi P. S., 2013, *ApJ*, **771**, 30
- Robertson B. E., Ellis R. S., Furlanetto S. R., Dunlop J. S., 2015, *ApJ*, **802**, L19
- Rodighiero G., Vaccari M., Franceschini A., et al., 2010, *A&A*, **515**, A8
- Rubin K. H. R., Prochaska J. X., Koo D. C., Phillips A. C., Martin C. L., Winstrom L. O., 2014, *ApJ*, **794**, 156
- Sajina A., Yan L., Fadda D., Dasyra K., Huynh M., 2012, *ApJ*, **757**, 13
- Scherrer R. J., Bertschinger E., 1991, *ApJ*, **381**, 349

- Schneider P., 2010, *Extragalactic Astronomy and Cosmology: An Introduction*, doi:10.1007/978-3-642-54083-7.
- Seljak U., 2000, *MNRAS*, **318**, 203
- Shang C., Haiman Z., Knox L., Oh S. P., 2012, *MNRAS*, **421**, 2832
- Springel V., Hernquist L., 2003, *MNRAS*, **339**, 289
- Thacker C., Cooray A., Smidt J., et al., 2013, *ApJ*, **768**, 58
- The CORE Collaboration Armitage-Caplan C., Aveliz M., Barbosa D. a., 2011, arXiv:1102.2181,
- Tinker J. L., Wetzel A. R., 2010, *ApJ*, **719**, 88
- Tinker J. L., Kravtsov A. V., Klypin A., Abazajian K., Warren M., Yepes G., Gottlöber S., Holz D. E., 2008, *ApJ*, **688**, 709
- Tinker J. L., Robertson B. E., Kravtsov A. V., Klypin A., Warren M. S., Yepes G., Gottlöber S., 2010, *ApJ*, **724**, 878
- Utomo D., Kriek M., Labbé I., Conroy C., Fumagalli M., 2014, *ApJ*, **783**, L30
- Veilleux S., Cecil G., Bland-Hawthorn J., 2005, *ARA&A*, **43**, 769
- Viero M. P., Ade P. A. R., Bock J. J., et al., 2009, *ApJ*, **707**, 1766
- Viero M. P., Wang L., Zemcov M., et al., 2013a, *ApJ*, **772**, 77
- Viero M. P., Moncelsi L., Quadri R. F., et al., 2013b, *ApJ*, **779**, 32
- Wechsler R. H., Zentner A. R., Bullock J. S., Kravtsov A. V., Allgood B., 2006, *ApJ*, **652**, 71
- Weiner B. J., Coil A. L., Prochaska J. X., et al., 2009, *ApJ*, **692**, 187
- Wetzel A. R., Tinker J. L., Conroy C., 2012, *MNRAS*, **424**, 232
- Xia J.-Q., Negrello M., Lapi A., De Zotti G., Danese L., Viel M., 2012, *MNRAS*, **422**, 1324
- Yan L., et al., 2005, *ApJ*, **628**, 604

APPENDIX A: SUMMARY OF PARAMETERS

Table A1 summarizes the parameters in the gas regulator model. Table A2 lists the parameter constraints, and Table A3 shows the correlation matrix of these parameters. Figure A1 shows the 1-D and 2-D posterior distribution from the MCMC chains.

APPENDIX B: COMPLETE FIGURES OF COMPARISONS BETWEEN OBSERVATIONS AND OUR MODEL

Most figures in the main text only show a single band or redshift slice for the purpose of demonstration. In this appendix, we show the full comparison we have conducted.

- Figure B1: our fit to the *Planck* power spectra of CFIRB.
- Figure B2: our model prediction for the *Herschel* power spectra of CFIRB.
- Figure B3: our model prediction for the correlation between CFIRB and CMB lensing potential.
- Figure B4: our model prediction for the redshift distribution of CFIRB emission.
- Figure B5: our model prediction for the bolometric IR luminosity functions.
- Figure B6: our model prediction for the FIR flux density functions (number counts).

This paper has been typeset from a \LaTeX file prepared by the author.

Parameter	Meaning	Fiducial value	Reference
Cosmic accretion			
f_b	Ω_b/Ω_M	0.18	Planck Collaboration XVI (2014)
f_{ga}	(gas mass) / (gas mass + stellar mass) in cosmic accretion, $0 < f_{\text{ga}} < 1$	(0.8)	Dekel & Mandelker (2014)
\dot{M}_a	Accretion rate of <i>all</i> baryon mass	–	ibid.
p	Penetration factor, $M_{\text{accreted baryon}}/(f_b M_{\text{accreted DM}})$	(0.5)	ibid.
Star formation			
K	$L_{\text{IR}} = \text{SFR}/K$	1.7×10^{-10}	Kennicutt (1998)
\dot{M}_{sf}	Star formation rate (SFR)	–	Dekel & Mandelker (2014)
t_{sf}	Star formation time scale $t_{\text{sf}} = \epsilon^{-1} t_d$	–	ibid.
ϵ	SFR efficiency per dynamical time	0.02	ibid.
t_d	Dynamical time, $t_d = \nu_d t$, where t is the cosmic time	–	ibid.
ν_d	t_d in units of the cosmological time	0.0071	ibid.
R	Fraction of gas mass returned by star formation	(0.46)	ibid.
η	Mass loading factor, ratio between gas outflow and SFR	–	Eq. 16
Metal and dust			
y	Metal yield	(0.016)	Lilly et al. (2013)
r	Dust-to-metal mass density ratio	(0.4)	Hayward et al. (2011)
Dust SED			
β	spectral index of dust SED	(2)	ibid.
κ	dust opacity, $\kappa = \kappa_0(\nu/\nu_0)^\beta$	–	Hayward et al. (2011)
κ_0	opacity at the pivot frequency	0.050	ibid.
ν_0	pivot frequency for opacity	$850\mu\text{m}$	ibid.
Halo mass – IR luminosity relation			
M_{pk}	Peak halo mass for star formation rate	–	Eq. 16
M_{min}	Minimum halo mass for hosting a FIR galaxy	–	Eq. 11

Table A1. Parameters in the gas regulator model. Numbers in parentheses indicate the values used in the references; these parameters are set free in our model.

Parameter	Prior	Constraint (68%)	Definition	Equation
η_0	[0, 1]	$0.44^{+0.03}_{-0.02}$	Minimum value of mass loading factor (at M_{pk})	16
α_1	[0, 5]	$2.3^{+0.2}_{-0.2}$	Slope of mass loading factor for low-mass end ($\eta \propto M^{-\alpha_1}$)	16
α_2	[0, 3]	$0.67^{+0.04}_{-0.04}$	Slope of mass loading factor for high-mass end ($\eta \propto M^{\alpha_2}$)	16
β	[1, 3]	$2.1^{+0.04}_{-0.03}$	Spectral index for dust opacity	14
σ	[0.2, 2]	$0.88^{+0.05}_{-0.05}$	Logarithmic scatter of L_{IR} at a given halo mass	27
z_0	[0, 3]	$0.68^{+0.04}_{-0.05}$	Extra redshift dependence of accretion rate	9
δ_1	[0, 5]	$2.2^{+0.2}_{-0.2}$	Extra redshift dependence of accretion rate	9
δ_2	[-3, 3]	$1.1^{+0.06}_{-0.06}$	Extra redshift dependence of accretion rate	9
f_{gap}	[0, 1]	$0.57^{+0.03}_{-0.03}$	Product of the gas mass fraction and the penetration factor	1
yr	[0.0001, 0.01]	$0.0033^{+0.0002}_{-0.0002}$	Product of metal yield and dust-to-metal ratio	12
q	[0, 1]	$0.92^{+0.05}_{-0.05}$	Quenching factor for satellite galaxies	20
μ	[0, 1]	$0.61^{+0.04}_{-0.04}$	$(1 - R)$, where R is the return fraction	1
$\log_{10}M_{\text{min}}$	[9, 11]	$10^{+0.6}_{-0.6}$	Minimum halo mass for hosting IR galaxies	11
$\log_{10}M_{\text{pk}}$	[11, 13]	$12^{+0.04}_{-0.05}$	Peak mass of star formation efficiency	16

Table A2. Constraints on the model parameters.

	η_0	α_1	α_2	β	σ	z_0	δ_1	δ_2	f_{gap}	ry	q	μ	$\log_{10}M_{\text{min}}$	$\log_{10}M_{\text{pk}}$
η_0	1	-0.047	-0.27	0.026	0.069	-0.095	-0.064	0.18	0.46	0.34	0.08	0.057	0.049	-0.13
α_1	-0.047	1	-0.1	0.061	-0.092	-0.043	0.01	-0.062	0.15	-0.031	0.016	-0.027	0.0038	-0.32
α_2	-0.27	-0.1	1	-0.083	-0.18	-0.21	-0.067	-0.24	0.34	0.045	0.13	0.061	-0.01	0.52
β	0.026	0.061	-0.083	1	0.1	-0.024	-0.029	-0.35	-0.085	0.15	-0.022	0.14	0.00052	-0.12
σ	0.069	-0.092	-0.18	0.1	1	-0.12	-0.013	-0.49	0.071	-0.3	0.045	-0.19	-0.023	-0.84
z_0	-0.095	-0.043	-0.21	-0.024	-0.12	1	-0.013	0.17	0.27	-0.024	0.051	-0.039	0.016	0.064
δ_1	-0.064	0.01	-0.067	-0.029	-0.013	-0.013	1	-0.017	-0.058	-0.029	0.0065	-0.0047	0.0027	0.00098
δ_2	0.18	-0.062	-0.24	-0.35	-0.49	0.17	-0.017	1	-0.3	-0.26	0.075	-0.068	0.021	0.33
f_{gap}	0.46	0.15	0.34	-0.085	0.071	0.27	-0.058	-0.3	1	0.15	-0.036	0.22	0.032	0.0027
ry	0.34	-0.031	0.045	0.15	-0.3	-0.024	-0.029	-0.26	0.15	1	0.048	-0.27	0.026	0.3
q	0.08	0.016	0.13	-0.022	0.045	0.051	0.0065	0.075	-0.036	0.048	1	0.079	-0.012	-0.0082
μ	0.057	-0.027	0.061	0.14	-0.19	-0.039	-0.0047	-0.068	0.22	-0.27	0.079	1	0.0034	0.19
$\log_{10}M_{\text{min}}$	0.049	0.0038	-0.01	0.00052	-0.023	0.016	0.0027	0.021	0.032	0.026	-0.012	0.0034	1	0.014
$\log_{10}M_{\text{pk}}$	-0.13	-0.32	0.52	-0.12	-0.84	0.064	0.00098	0.33	0.0027	0.3	-0.0082	0.19	0.014	1

Table A3. Correlation matrix for the model parameters.

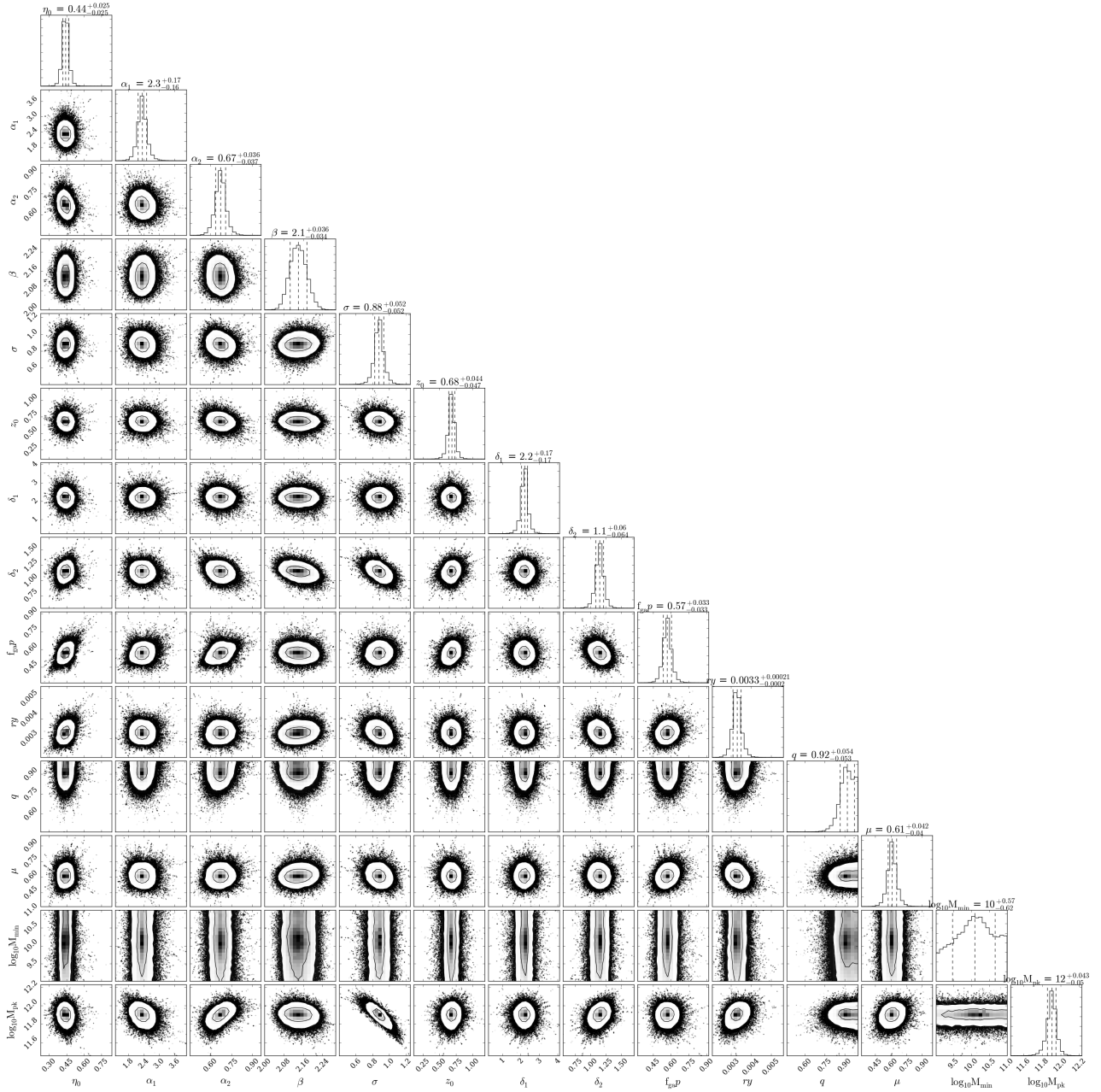


Figure A1. The 68% and 95% constraints of our model parameters. The diagonal panels show the posterior distribution and the 68% constraint of each parameter.

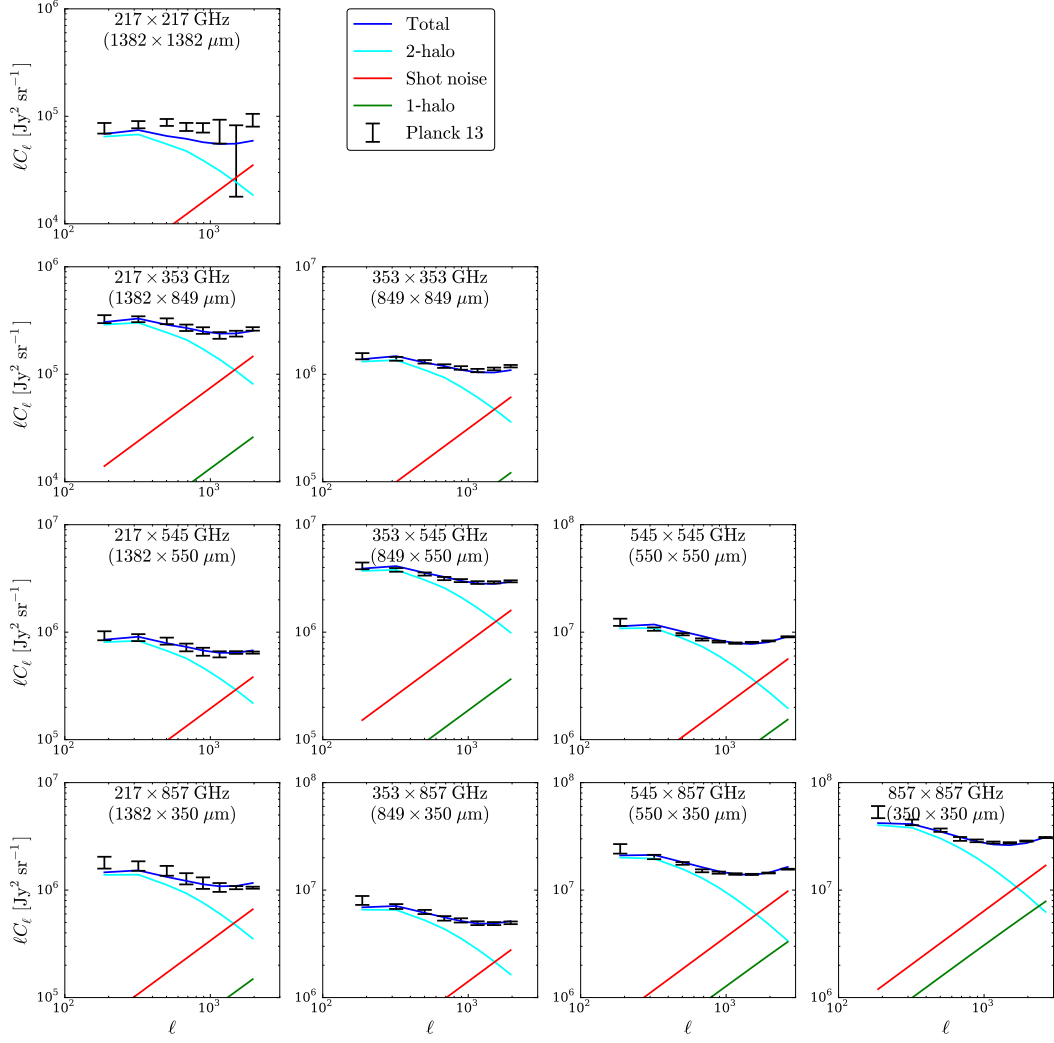


Figure B1. Our model fitting to the CFIRB power spectra from *Planck*.

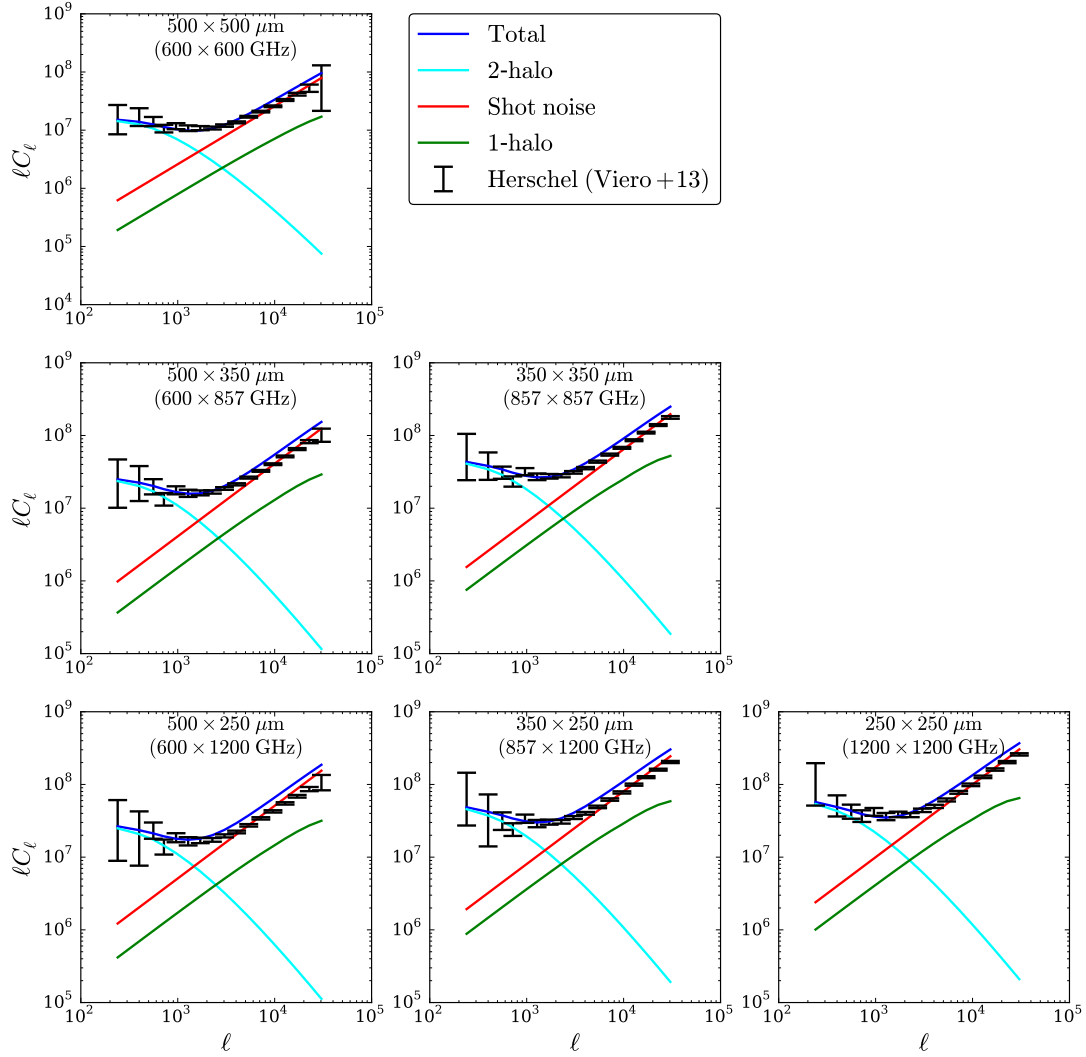


Figure B2. CFIRB power spectra from *Herschel*-SPIRE (see Section 5.5) compared with our model prediction.

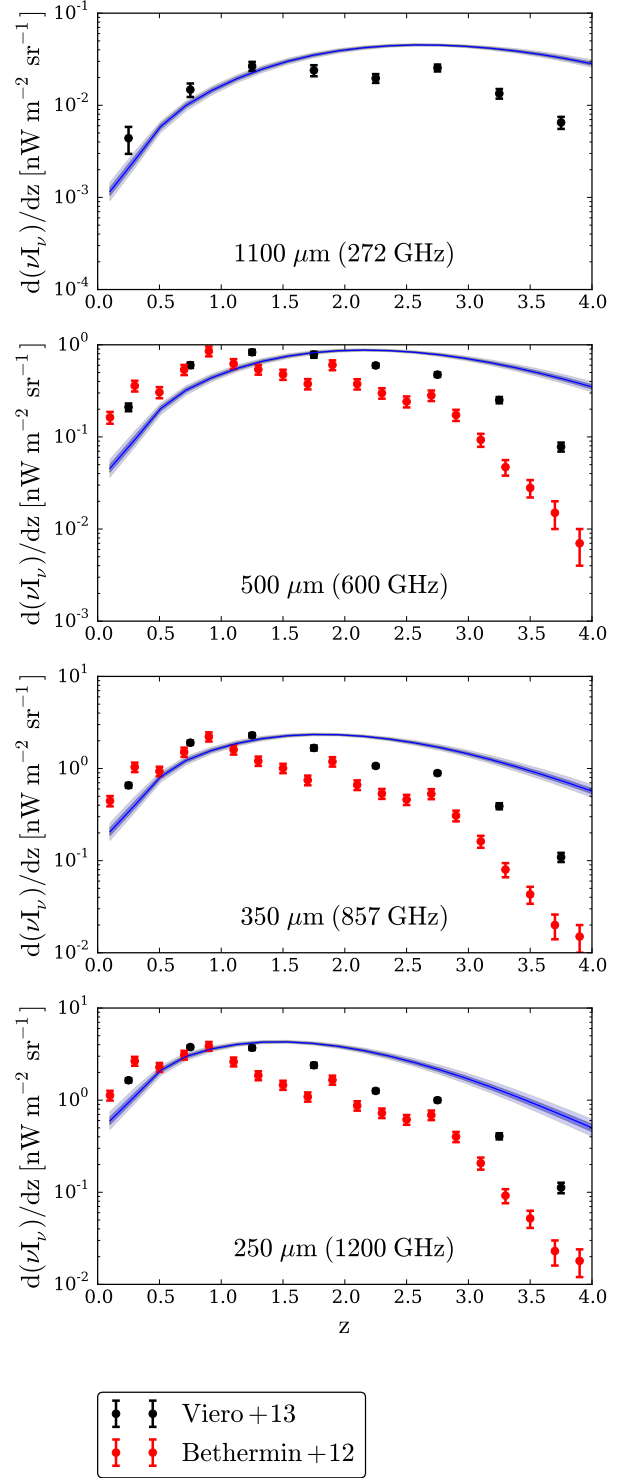
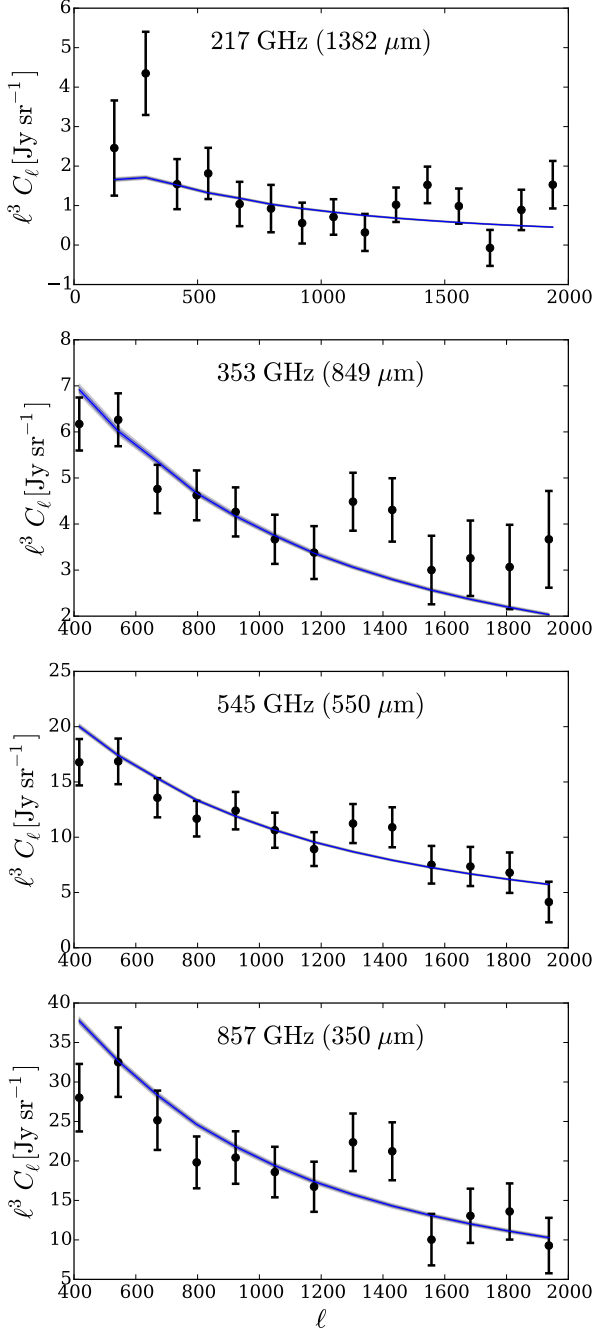


Figure B3. Correlation between CFIRB and CMB lensing potential (see Section 5.1) compared with our model prediction.

Figure B4. Redshift distribution of CFIRB (see Section 5.4) compared with our model prediction.

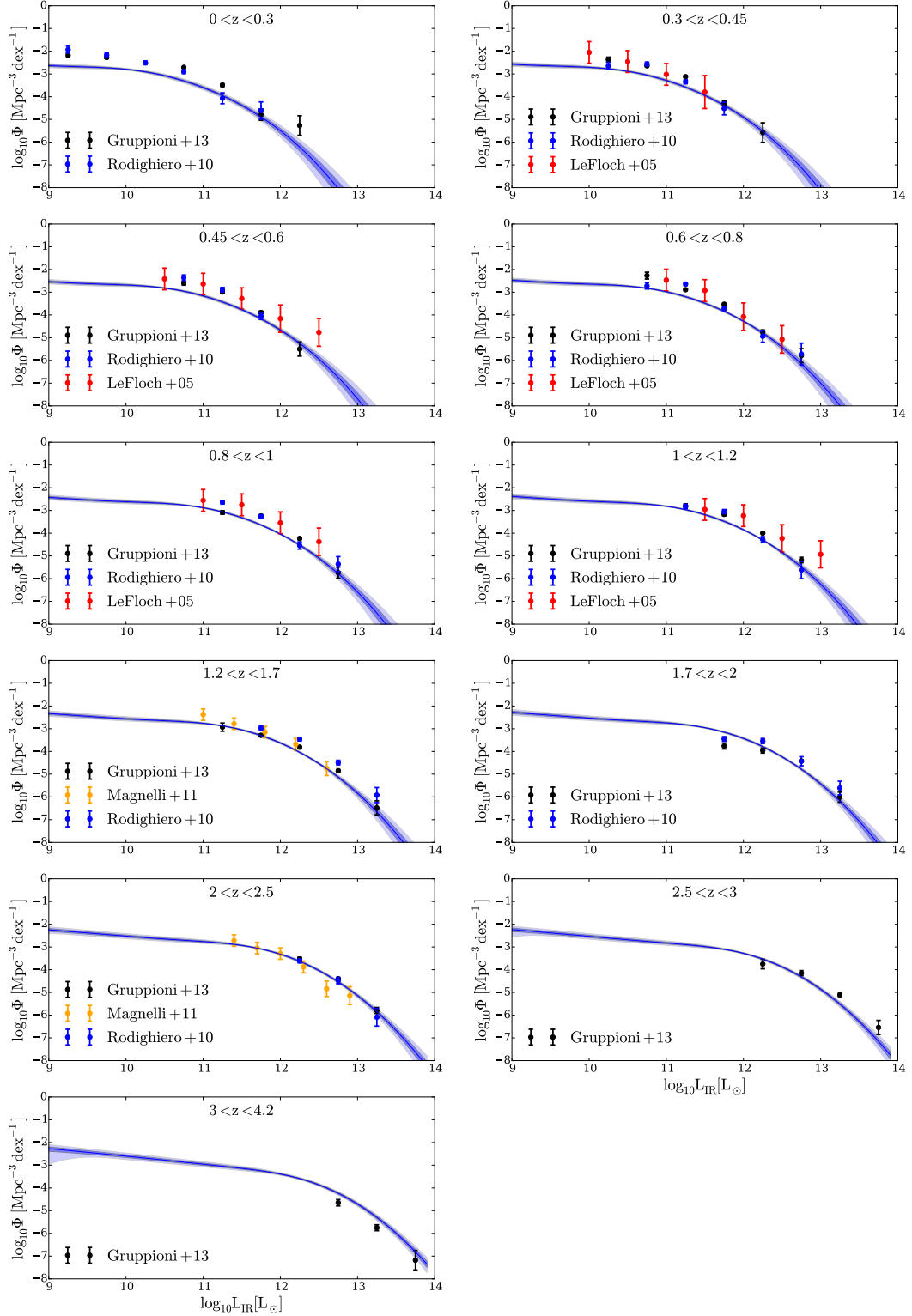


Figure B5. Bolometric infrared luminosity functions (see Section 5.2) compared with our model prediction.

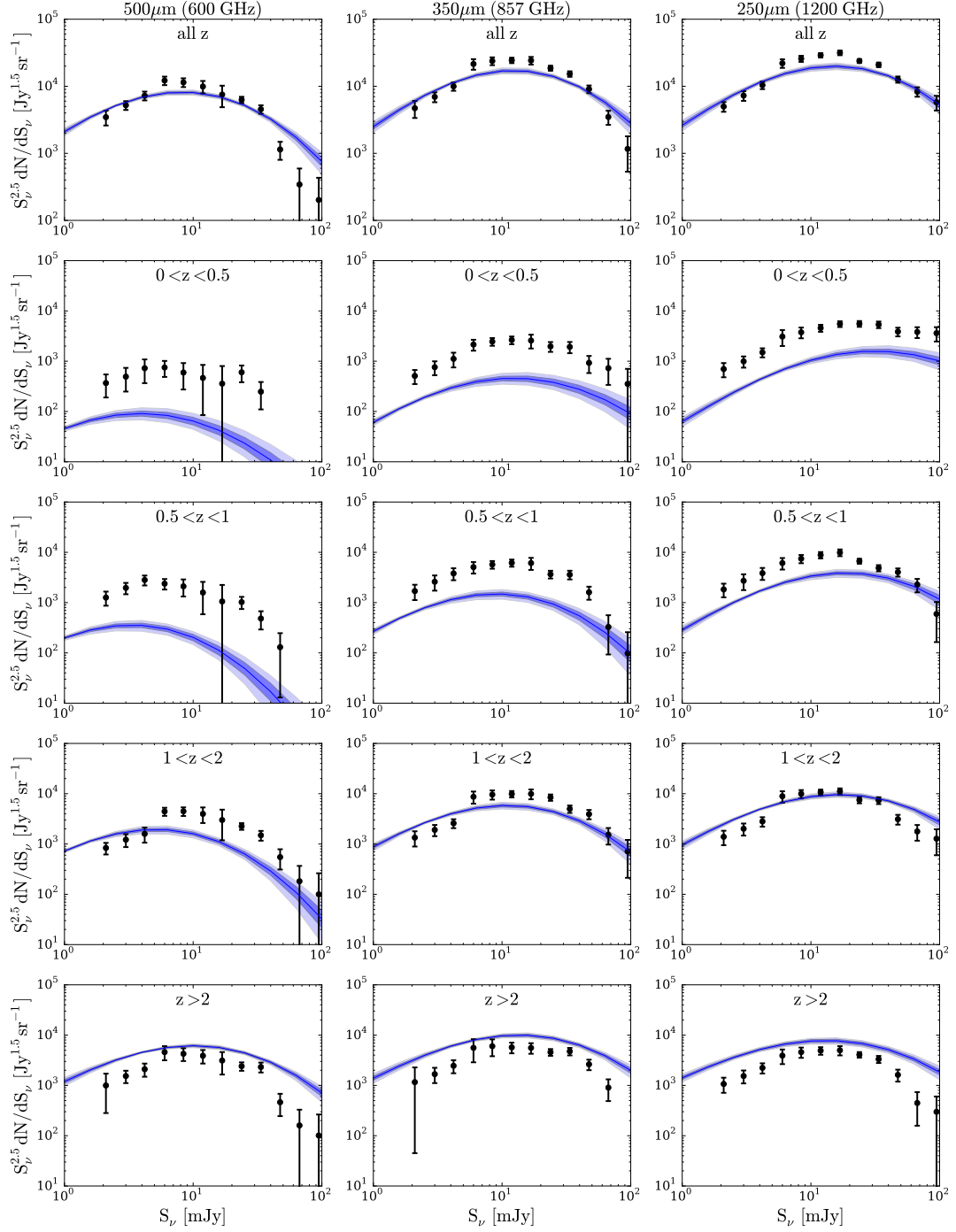


Figure B6. Number counts data from Béthermin et al. (2012, see Section 5.3) compared with our model prediction.